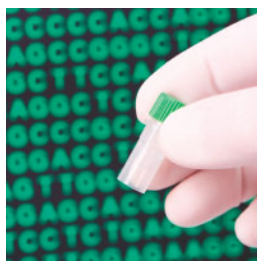# RESEARCH WATCH

Pharmacogenomics

Major finding: *VEGFR3* and *CYP3A5* polymorphisms predict sunitinib response and toxicity.

Approach: An observational, prospective study was performed in previously untreated RCC patients.

Impact: Genetic markers may be used to predict efficacy and toxicity of sunitinib.

SNPs PREDICT SUNITINIB TREATMENT OUTCOME IN RCC

Renal cell carcinoma (RCC), the most common type of kidney cancer in adults, is resistant to both chemotherapy and radiation therapy. Sunitinib malate, an orally administered tyrosine kinase inhibitor with activity against VEGF receptor (VEGFR), has been shown to increase progression-free survival (PFS) in patients with advanced clear-cell RCC and is currently a standard treatment option. However, a subset of patients fails to respond to therapy or develops treatment-limiting toxicity. Garcia-Donas and colleagues hypothesized that genetic polymorphisms among patients may serve as biomarkers that can predict response or toxicity to sunitinib. Previously untreated patients with clear-cell RCC were enrolled in an observational, prospective study that assessed response, PFS, and toxicity to sunitinib in relation to single-nucleotide polymorphisms (SNP) in nine genes thought to be potentially involved in sunitinib action, metabolism, or transport. Interestingly, two *VEGFR3* polymorphisms were associated with a shorter PFS, and one functional *CYP3A5* polymorphism was associated with increased risk of sunitinib dose reduction secondary to toxic effects. These findings provide relevant insight into the pharmacodynamics and pharmacokinetics of sunitinib, as VEGFR3 is a direct target and CYP3A5 is a member of the cytochrome P450 family of enzymes involved in drug metabolism. Together, the data represent an important advance in personalized medicine, and with additional validation, potentially may be used to identify which RCC patients will benefit from treatment with sunitinib. ■

Garcia-Donas J, Esteban E, Leandro-García LJ, Castellano DE, del Alba AG, Climent MA, et al. Single nucleotide polymorphism associations with response and toxic effects in patients with advanced renal-cell carcinoma treated with first-line sunitinib: a multicentre, observational, prospective study. Lancet Oncol 2011;12:1143–50.

Personalized Medicine

Major finding: Differential changes in death and survival signaling underlie oncogene addiction.

Impact: A simple, noninvasive method can identify patients who may benefit from targeted therapy.

Approach: Mathematical modeling is combined with imaging to predict oncogene addiction.

MATHEMATICAL MODELING CAN IDENTIFY ONCOGENE-ADDICTED TUMORS

It remains unclear which cellular properties underlie a tumor's dependence on a single oncogenic signaling pathway. Tran and colleagues sought to elucidate the general underlying mechanisms of oncogene addiction with the ultimate goal of developing a strategy to quickly determine whether oncogene-targeted treatment will be effective. First, using a mouse model of *Kras*-addicted lung cancer, they combined immunohistochemistry of several prosurvival and prodeath effector molecules at multiple time points before and after *Kras* inactivation with the proliferative and apoptotic indices to generate an ordinary differential equation model of aggregate survival and death signals over time. This model fit serial imaging data and showed that the response of oncogene-addicted tumors could be explained almost entirely by a sharp attenuation of the survival signal and a more gradual decline in the death signal. The authors also used this model to successfully predict the effects of particular prosurvival (Stat, Akt) and prodeath (p53) pathways on oncogene-addicted tumor growth, and to predict the effect of *Myc* inactivation in *Myc*-addicted murine lymphoma, suggesting that this model is applicable to oncogene-addicted tumors regardless of oncogene or tumor type. The authors then used serial imaging data to determine whether tumor growth and regression kinetics were sufficient for a support vector machine (SVM) learning algorithm to distinguish an oncogene-addicted genotype. After only the first 2 weekly scans following oncogene inactivation in either *Kras*-addicted or *Myc*-induced (but not addicted) murine lung cancers, the SVM could successfully classify tumors. Using the mouse SVM classifier on CT scan imaging data from lung cancer patients treated with erlotinib, the authors were able to predict the *EGFR* genotype and progression-free survival of patients after 4 weekly CT scans. Although *EGFR* mutational status is a known predictor of response to erlotinib, it is not always possible to obtain a sample for biopsy or screen for *EGFR* mutations. Quantitative imaging algorithms may therefore aid in the personalized management of patients treated with targeted therapies. ■

Tran PT, Bendapudi PK, Lin HJ, Choi P, Koh S, Chen J, et al. Survival and death signals can predict tumor response to therapy after oncogene inactivation. Sci Transl Med 2011;3:103ra99.

Cancer Research

AACR

Highlights from Recent Cancer Literature

Updated Version	Access the most recent version of this article at: http://cancerres.aacrjournals.org/content/71/22/6913

E-mail alerts	Sign up to receive free email-alerts related to this article or journal.
Reprints and Subscriptions	To order reprints of this article or to subscribe to the journal, contact the AACR Publications Department at pubs@aacr.org.
Permissions	To request permission to re-use all or part of this article, contact the AACR Publications Department at permissions@aacr.org.

Breaking Advances
Highlights from Recent Cancer Literature

Killer Activity Enhanced

T cells that express the cell-surface marker CD8 have undoubted potential to recognize and destroy malignant cells expressing cognate antigens. For some human cancers, the more CD8^{+} T cells in a tumor microenvironment, the better the patient's prognosis. However, by the time most cancers are detected, there may not be enough of these *useful* cells to have a major clinical impact. One treatment approach has been to harvest T cells from a patient, expand them in the presence of a cocktail of cytokines, and return the T cells to the patient in the hope that they may generate specific anticancer immunity. Although this strategy works in some instances, it is usually ineffective, not least because the malignant cells acquire resistance to the killing methods used by CD8^{+} T cells. de Bruyn and colleagues have described novel methods leading to 500-fold increased killing potential of CD8^{+} T cells, and these novel methods are easily translatable to the clinic. This novel strategy targeted one particular killing molecule—TNF-related apoptosis-inducing ligand (TRAIL)—to the T-cell surface. This resulted in greatly enhanced ability of T cells to kill targeted malignant cell lines and primary cells from cancer patients at a ratio of 2:1 T cells to malignant cells; without TRAIL, it took a ratio of 100:1 T cells to malignant cells to achieve similar results. The authors tried 2 different approaches: (i) an anti-CD3:TRAIL, in which the anti-CD3 component also played a role in activating T cells, and in which the killing mechanism involved granzyme and perforin; and (ii) K12:TRAIL, which functioned by activation of caspases in malignant cells. Results from the *in vitro* and *in vivo* xenograft experiments suggest that anti-CD3:TRAIL may be particularly useful for *ex vivo* tumor cell purging of bone marrow, or for tumors in anatomically confined regions. In contrast, results from the K12:TRAIL approach show enhanced graft-versus-tumor responses without causing detrimental graft-versus-host disease. The K12:TRAIL approach could be further varied with the use of TRAIL fusion proteins incorporating other immunomodulatory ligands or antibody fragments. To this end, the authors suggest other ways to simultaneously stimulate T cells and add another killing molecule to their surface. (*Image courtesy of MorgueFile.*)

de Bruyn M, Wei Y, Wiersma VR, Samplonius DF, Klip HG, van der Zee AG, et al. Cell surface delivery of TRAIL strongly augments the tumoricidal activity of T cells. Clin Cancer Res 2011;17:5626–37.

Tumor-Entrained Neutrophils Block Metastatic Spread in Breast Cancer

Cells of the immune system can serve as friends or foes with regard to cancer development. A prevailing model suggests that immune surveillance is triumphant at an early stage of tumor formation, with advanced cancers generally entraining the immune system to drive malignancy. To clarify the role of immunosurveillance in breast cancer metastases, Granot and colleagues implanted breast cancers orthotopically in mice and performed microarray analyses of liver and lung tissues. A number of neutrophil-specific genes were expressed in lung, but not liver. Depletion of neutrophils blocked metastases, indicating that neutrophil seeding of the lungs blocked establishment of metastases. Subsequent experiments showed that neutrophils were entrained through secretion of CCL2, and blocked malignant cells through production of H_2O_2. Similar tumor-entrained neutrophils were also isolated from women with newly diagnosed breast cancer. These results suggest that neutrophils are co-opted by primary breast cancers to block spread to metastatic sites. (*Image courtesy of L.M. Coussens, University of California, San Francisco.*)

Granot Z, Henke E, Comen EA, King TA, Norton L, Benezra R. Tumor entrained neutrophils inhibit seeding in the premetastatic lung. Cancer Cell 2011;20:300–14.

A Germline Variant in p53 Confers Susceptibility to Basal Cell Carcinoma, Prostate Carcinoma, and Glioma

Basal cell carcinoma is a very common skin cancer associated with sun exposure and with mutations in genes regulating Sonic Hedgehog signaling. To identify candidate susceptibility genes, Stacey and colleagues performed a genome-wide association study of 1,400 affected individuals and 30,000 controls in the Icelandic population, using single-nucleotide polypeptide arrays, with whole-genome sequencing of 460 additional individuals. They identified a strong signal (OR, 2.36; $P = 5.2 \times 10^{-17}$) in the 3' untranslated region of *TP53*, which was subsequently confirmed in non-Icelanders, albeit at frequencies below the 0.019 level found in Icelanders. This variant, which leads to impaired 3' processing of *TP53* through modification of the polyA sequence, was also associated with susceptibility to prostate cancer (OR, 1.63; $P = 1.1 \times 10^{-4}$) and to glioma (OR, 2.35; $P = 1.0 \times 10^{-5}$), but not for breast cancer, a malignancy linked to mutation in *p53*, which leads to gain of function in this tumor-suppressor gene.

Stacey SN, Sulem P, Jonasdottir A, Masson G, Gudmundsson J, Gudbjartsson DF, et al. A germline variant in the TP53 polyadenylation signal confers cancer susceptibility. Nat Genet 2011; 43:1098–103.

Macrophages Block Death of Metastatic Breast Cancer Cells

Metastatic breast carcinoma cells exhibit increased expression of vascular cell adhesion molecule-1 (VCAM-1), but the functional consequence of this increased expression has remained enigmatic. A recent report by Chen and colleagues has revealed a prosurvival function for VCAM-1–positive breast carcinoma cells in tumor microenvironments heavily infiltrated by myeloid cells, specifically macrophages expressing α4-integrins. Interaction of macrophage α4-integrin with VCAM-1 resulted in VCAM-1 membrane clustering and subsequent EZRIN-dependent triggering of AKT

activation, which in turn resulted in a prosurvival signal for breast carcinoma cells that metastasized to the lung. Significantly, blockade of interaction between VCAM-1 and α4-integrin enhanced apoptotic activity after exposure to proapoptotic cytokines including TRAIL. Together, these data indicate that breast carcinoma cells metastasize in part by co-opting a physiologic mechanism that enables them to increase their survival by interacting with macrophages in their local tumor microenvironments. These results illustrate how innate immune cells can causally contribute to metastasis by providing a survival advantage to cells that carry a receptor eliciting a prosurvival advantage. Hence, targeting of tumor cell and leukocyte interactions may provide a novel approach for preventing penultimate stages of cancer progression, namely metastasis. (*Image courtesy of MorgueFile.*)

Chen Q, Zhang XH, Massagué J. Macrophage binding to receptor VCAM-1 transmits survival signals in breast cancer cells that invade the lungs. Cancer Cell 2011;20:538–49.

Mathematical Models for Predicting Drug Responses of Tumors

The ability to predict when targeting the inactivation of a gene product will result in tumor regression would be highly useful for development of new anticancer therapeutics. Tran and colleagues used a computational biologic approach to develop methods for predicting when malignant cells are addicted to oncogenes with the hope that this strategy could inform development and clinical use of targeted therapeutics. To start, they showed the utility of the mathematical model for predicting when oncogene inactivation would result in tumor regression, using transgenic mouse models of tumor progression to evaluate survival and death signals in malignant cells. Surprisingly, they found that both types of signals decreased upon oncogene inactivation, but the former decreased more quickly, when a tumor is poised to regress. This response was similar to the "oncogenic shock" model proposed by other investigators. Next, the investigators showed the utility of their mathematical modeling approaches to predict when inhibition of epidermal growth factor receptor activation would result in regression of tumors in patients with adenocarcinoma, thus providing an example of the increasing feasibility for *in silico* modeling of pathophysiologic processes. Further work is required to discern whether these approaches can be used prospectively to predict the efficacy of a targeted therapeutic, and whether they can be applied to combined therapies as well as single agents. (*Image courtesy of MorgueFile.*)

Tran PT, Bendapudi PK, Lin HJ, Choi P, Koh S, Chen J, et al. Survival and death signals can predict tumor response to therapy after oncogene inactivation. Sci Transl Med 2011;3:103ra99.

Note: *Breaking Advances* are written by *Cancer Research* Editors. Readers are encouraged to consult the articles referred to in each item for full details on the findings described.

TARGETED THERAPIES

Model reveals addiction to oncogenes

Targeted therapies can produce dramatic responses in some patients, but in many cases it is difficult to tell who will respond and who will not. A mathematical model of survival and death signals has predicted which lung cancer tumors will respond to the EGFR tyrosine kinase inhibitor erlotinib, pointing the way to a more-informed use of this drug, and other drugs targeting oncogene addiction in cancer.

The Felsher laboratory has been studying the phenomenon of oncogene addiction for over 10 years. Based on this research, "we believed that it should be possible to 'model' oncogene addiction and thereby predict when oncogene addiction will occur," explains Felsher.

The researchers teamed up with members of the Paik laboratory, who specialize in the measurement, quantification, analysis and modeling of imaging data. As Felsher outlines, "we decided together that we could 'model' imaging combined with cell signaling data to attempt to predict and define oncogene addiction."

The team studied conditional mouse models of lung cancer and lymphoma using imaging and assessed biomarkers associated with proliferation and apoptosis. From these data they developed a mathematical model based on ordinary differential equations that predicted oncogene addiction from the differential changes in survival and cell death signals.

Crucially, the investigators were able to use this model and imaging to predict oncogene addiction and, therefore, responses of patients with lung cancer who received erlotinib as part of a clinical trial.

Going forward, Felsher says, "we plan to improve our model by incorporating other variables such as the role of self-renewal, senescence and home immune contributions and to prospectively test our models in a clinical study."

Rebecca Kirk

Original article Tran, P. T. *et al*. Survival and death signals can predict tumor response to therapy after oncogene inactivation. *Sci. Transl. Med.* **3**, 103ra99 (2011)

ONCOGENE ADDICTION

Striking a Balance Between Feasible and Realistic Biological Models

Andrea Califano[1,2,3,4,5,6]

The fusion of empirical science with large-scale computing platforms has allowed rapid advances in our ability to model physiological and pathophysiological processes in silico. In this week's issue of *Science Translational Medicine*, Tran *et al*. present a simple framework for the quantitative modeling of oncogene addiction that provides mechanistic insights into tumor biology.

The golden ages of several sciences—from chemistry, to physics, to economics—have invariably coincided with the ability to complement their empirical foundation with quantitative analytical models that could predict the results of a "thought experiment" (gedankenexperiment) without the need to actually perform it. For instance, chemistry experienced major development as a discipline following the formulation of some of its basic quantitative principles, such as the conservation of mass proposed by Antoine Lavoisier at the end of the 18th century. Often, a second period of expansion has resulted when computing power allowed the simulation of complex quantitative models that could not be solved analytically.

In biology and medicine, the use of quantitative models is relatively recent and has occurred at a juncture when large-scale computing platforms are already ubiquitously available and genome-scale experimental techniques that generate the massive amounts of data necessary for quantitative modeling are achieving maturity. This suggests that the golden age of biology may be imminent, spurred by our growing ability to model physiological and pathophysiological processes in silico. In this context, Tran and colleagues present, in this week's issue of *Science Translational Medicine,* an elegant and startlingly simple framework for the quantitative modeling of oncogene addic-

tion (*1*). Despite its simplicity, this model yields all but simple results and creates the prerequisites to understand this phenomenon at a more quantitative and predictive level. Such an endeavor could not be timelier, because the elucidation of oncogene addiction mechanisms was recently listed as one of the "big questions" by the homonymous initiative launched by Harold Varmus, the recently appointed director of the U.S. National Cancer Institute (*2*).

Tran *et al.* started from the empirical observation first suggested by Weinstein in 2002 (*3*) that cancers can exhibit dramatic regression upon inhibition of relevant oncogenes. Such a premise constitutes the rationale behind the majority of nonchemotoxic (that is, molecularly targeted) therapeutic approaches for cancer currently used in the clinic, such as the drugs trastuzumab, erlotinib, and imatinib, which are used to treat *HER2*-amplified breast tumors (*4*), *EFGR*-amplified lung cancers (*5*), and *BCR-ABL* fusion gene–driven chronic myelogenous leukemia (CML) (*6*), respectively. Although the precise mechanisms that underlie oncogene addiction are still largely elusive, Tran and colleagues proposed that aberrant activation of oncogenes, such as *MYC* or *K-Ras*, ultimately disrupts the competitive balance between pro-survival and pro-death signals in the cell. Thus, the ability to quantitatively model the competition between these programs may help us to better understand oncogene addiction and predict its effect on tumor regression.

On the basis of this hypothesis, the authors used distinct quantitative readouts—imaging and in situ biomarkers of proliferation and apoptosis—to characterize the responses of pro-survival and pro-death signals to oncogene inactivation. Despite its simplicity, their corresponding ordinary differential equation (ODE) model was ef-

fective in representing and predicting the differential dynamics of several pro-survival and pro-death signaling factors [phosphorylated extracellular signal–regulated kinase 1 (Erk1) and Erk2, the serine/threonine-protein kinase Akt1, signal transducer and activator of transcription 3 (Stat3) and Stat5, and the mitogen-activated protein kinase p38] that contribute to the aggregate cellular survival and death signals after oncogene inactivation. More importantly, the model was extended to predict the relevance of specific genetic alterations, including homozygous deletion of the gene that encodes the tumor suppressor protein p53 (*p53*^{−/−}), activating mutations in the *STAT3* gene that specify a constitutively activated version of the Stat3 protein (STAT3-d358L), and mutations in the *AKT1* gene that give rise to constitutively activated Akt1 (myr-Akt1). Although this is a small subset of oncogene-addiction modulators, this analysis constitutes proof-of-concept for the systematic representation of a much larger repertoire of germline and somatic alterations that define the genetic landscape of a cancer cell and mediate its response to oncogene inactivation.

Furthermore, the model was highly effective in predicting progression-free survival of lung cancer patients after erlotinib therapy, on the basis of the tumors' inferred *EGFR* genotypic landscape. These findings suggest that, using a relatively small number of genetic parameters, response to oncogene-inactivation therapy could be quantitatively predicted by treating pro-survival and pro-death signals as largely independent, with obvious potential application to personalized therapy.

MODELING LIFE AND DEATH

To model response of pro-survival and pro-death pathways to oncogene inactivation as a function of several modulating genetic events, Tran and colleagues used a transgenic mouse model with a doxycycline-inducible, *K-ras*[G12D]–activating mutation vector, which is known to induce lung adenocarcinoma that displays classic oncogene addiction. Lung-specific expression of *K-ras*[G12D] induced tumorigenesis in the lungs with a moderate latency of about 26 weeks. Removal of doxycycline from drinking water was sufficient to turn off the *K-ras*[G12D] promoter, thus simulating oncogene inactivation and allowing one to measure tumor growth and regression kinetics under a number of constraints, with the use of serial weekly microcomputer tomography

[1]Columbia Initiative in Systems Biology, Columbia University, New York, NY 10032, USA. [2]Center for Computational Biology and Bioinformatics, Columbia University, New York, NY 10032, USA. [3]Department of Biomedical Informatics, Columbia University, New York, NY 10032, USA. [4]Department of Biochemistry and Molecular Biophysics, Columbia University, New York, NY 10032, USA. [5]Institute for Cancer Genetics, Columbia University, New York, NY 10032, USA. [6]Herbert Irving Comprehensive Cancer Center, Columbia University, New York, NY 10032, USA.

E-mail: califano@c2b2.columbia.edu

(microCT) imaging. The ODE model that was inferred from this analysis not only has proven to be robust in the specific context of *K-Ras* addiction but also was used to extrapolate the analysis to *MYC*-addicted lymphomas, with good fit—a small deviation between predicted and observed results. These results suggest that overfitting (a classical statistical issue that occurs when the model fits the noise rather than the data) is not an issue in this case and that the model is generalizable to other oncogene-addiction scenarios.

A particularly interesting result of the model that could not have been predicted without a quantitative framework is that tumor remission does not appear to be driven either by an increase in apoptosis or by a decrease in proliferation alone. Rather, both pro-survival and pro-death signals are reduced after oncogene inactivation. Yet, the balance between the two signals is tilted to favor overall reduction in tumor mass. This could contribute to our mechanistic understanding of oncogene addiction, as has been similarly suggested on the basis of previous in vitro studies that used human tumor–derived cell lines (*7*). It also begs the question of whether the balance between these signals may be used to predict addiction in a more general set of therapeutic approaches that target a variety of oncogene and nononcogene dependencies in the cell, as well as their genetic modulators (Fig. 1).

THERAPY CRYSTAL BALL?
To address this question, Tran and colleagues performed an intriguing experiment to determine whether *MYC* oncogene addiction in lymphoma could be modulated by the ancillary genetic alterations described above—*p53*⁻/⁻, Stat3-d358L, and myr-Akt1—based only on the effects that these mutations have on pro-survival and pro-death signals.

Specifically, they tested whether independent measurement of pro-life and pro-death signals in cells that harbor the corresponding genetic alterations could recapitulate tumor growth when plugged into the previ-

Fig. 1. Predicting patient response. Although not an all-seeing crystal ball, the mathematical model devised by Tran *et al.* revealed, among other things, that anti-*MYC* therapy should be avoided in *p53*⁻/⁻ tumors, a finding that one day may aid in the design of personalized therapeutic approaches.

ous computational model. Interestingly, the authors' model effectively predicted the observed influences of these genetic manipulations. For instance, although Stat3-d358L and myr-Akt1 reduced apoptosis marginally in lymphoma cells and did not manage to tilt the survival-death signal balance after oncogene inactivation, *p53*⁻/⁻ had a major effect on apoptosis (75% abrogation of tumor cell death in *p53*⁻/⁻ tumors as compared with 19% in control cells without the p53 deletion), thus tilting the balance toward cancer cell survival and tumor growth after *MYC* inactivation. Therefore, the model showed that *p53*⁻/⁻ tumors are no longer addicted to *MYC*, which could have important consequences for treatment—for instance, by suggesting that anti-*MYC* therapy should be avoided in *p53*⁻/⁻ tumors, thus permitting the design of personalized therapeutic approaches once a suitable *MYC* inhibitor becomes available.

Will modeling of oncogene addiction by its effect on pro-survival and pro-death signals work for every tumor type? As the

authors themselves realize, probably not. Previous work from this group has shown that oncogene addiction involves restoration of cellular senescence as well as the shutdown of angiogenesis (*8*, *9*), and both of these mechanisms appear to be dependent on the host's immune system (*10*). Moreover, it is clear that different oncogenes contribute to tumorigenesis through disparate programs other than survival and death signaling. Indeed, many oncogenes are associated with alternative regulatory functions.

For example, translocation of a fragment of the *BCL6* gene in diffuse large B cell lymphoma (DLBCL) induces transcriptional inactivation of the gene that encodes Blimp1, a transcription factor that controls terminal B cell differentiation into plasma cells, leading to tumorigenesis. As a result, targeting *BCL6* in these tumors may not have a direct effect on pro-survival and pro-death signals, but it may simply induce terminal differentiation of tumor cells. Yet, because inhibition of pro-apoptotic and pro-senescence mechanisms coupled with activation of proliferative programs is a hallmark of many aggressive tumors, we expect that addiction to a large repertoire of oncogenes will directly impact these signals. This allows direct application of the computational framework introduced by Tran *et al.*

COMPLEX COMPUTING
Our current understanding of the biological mechanisms of tumorigenesis is built on more than 50 years of molecular cell biology research performed by a large number of investigators. In comparison, computational modeling of biological processes is a relatively recent discipline, practiced by only a handful of researchers. However, there is unmistakable evidence that computational models are becoming increasingly descriptive, accurate, and useful in elucidating cell processes and behavior at the molecular level (*11*–*14*). Such models have suggested that (i) cancer cells may not be uniquely addicted to oncogenes but can also be addicted to nononcogenes that encode proteins that imple-

ment tumor-specific regulatory bottlenecks (*15*) and (ii) such non-oncogene addictions may be exploited therapeutically (*16*). The first steps in predictive model–building endeavors will necessarily require construction of the cornerstone infrastructure of the discipline, on top of which more complex edifices of knowledge can be assembled.

To the expert biologist's eye, some of these initial constructions may fail to account for the full complexity and sophistication of the biological process they attempt to model. These initial structures may look more like primitive shacks, held together by duct tape, rather than elegant contemporary architectural wonders. However, these early efforts are necessary and should be encouraged, because they constitute the first obligatory step that leads to more sophisticated and realistic quantitative models that will ultimately recapitulate regulation of cellular processes. As a result, models such as those produced by Tran and colleagues should be applauded. They are simple enough to be analytically achievable and can be effectively simulated on today's computers. And yet, they provide valuable insight that could not be gleaned on a purely empirical basis.

REFERENCES AND NOTES

1. P. T. Tran, P. K. Bendapudi, H. J. Lin, P. Choi, S. Koh, J. Chen, G. Horng, N. P. Hughes, L. H. Schwartz, V. A. Miller, T. Kawashima, T. Kitamura, D. Paik, D. W. Felsher, Survival and death signals can predict tumor response to therapy after oncogene inactivation. *Sci. Transl. Med.* **3**, 103ra99 (2011).

2. J. Kaiser, Varmus targets 'dysfunction,' scientific barriers in cancer research. *ScienceInsider* (13 July 2010). http://news.sciencemag.org/scienceinsider/2010/07/varmus-targets-dysfunction.html.

3. I. B. Weinstein, Addiction to oncogenes—The Achilles heal of cancer. *Science* **297**, 63–64 (2002).

4. J. S. Ross, J. A. Fletcher, The *HER-2/neu* oncogene in breast cancer: Prognostic factor, predictive factor, and target for therapy. *Stem Cells* **16**, 413–428 (1998).

5. F. Ciardiello, G. Tortora, A novel approach in the treatment of cancer: Targeting the epidermal growth factor receptor. *Clin. Cancer Res.* **7**, 2958–2970 (2001).

6. B. J. Druker, S. Tamura, E. Buchdunger, S. Ohno, G. M. Segal, S. Fanning, J. Zimmermann, N. B. Lydon, Effects of a selective inhibitor of the Abl tyrosine kinase on the growth of Bcr-Abl positive cells. *Nat. Med.* **2**, 561–566 (1996).

7. S. V. Sharma, J. Settleman, Oncogene addiction: Setting the stage for molecularly targeted cancer therapy. *Genes Dev.* **21**, 3214–3231 (2007).

8. S. Giuriato, S. Ryeom, A. C. Fan, P. Bachireddy, R. C. Lynch, M. J. Rioth, J. van Riggelen, A. M. Kopelman, E. Passegué, F. Tang, J. Folkman, D. W. Felsher, Sustained regression of tumors upon MYC inactivation requires p53 or thrombospondin-1 to reverse the angiogenic switch. *Proc. Natl. Acad. Sci. U.S.A.* **103**, 16266–16271 (2006).

9. C. H. Wu, J. van Riggelen, A. Yetil, A. C. Fan, P. Bachireddy, D. W. Felsher, Cellular senescence is an important mechanism of tumor regression upon c-Myc inactivation. *Proc. Natl. Acad. Sci. U.S.A.* **104**, 13028–13033 (2007).

10. K. Rakhra, P. Bachireddy, T. Zabuawala, R. Zeiser, L. Xu, A. Kopelman, A. C. Fan, Q. Yang, L. Braunstein, E. Crosby, S. Ryeom, D. W. Felsher, CD4(+) T cells contribute to the remodeling of the microenvironment required for sustained tumor regression upon oncogene inactivation. *Cancer Cell* **18**, 485–498 (2010).

11. X. Yang, J. L. Deignan, H. Qi, J. Zhu, S. Qian, J. Zhong, G. Torosyan, S. Majid, B. Falkard, R. R. Kleinhanz, J. Karlsson, L. W. Castellani, S. Mumick, K. Wang, T. Xie, M. Coon, C. Zhang, D. Estrada-Smith, C. R. Farber, S. S. Wang, A. van Nas, A. Ghazalpour, B. Zhang, D. J. Macneil, J. R. Lamb, K. M. Dipple, M. L. Reitman, M. Mehrabian, P. Y. Lum, E. E. Schadt, A. J. Lusis, T. A. Drake, Validation of candidate causal genes for obesity that affect shared metabolic pathways and networks. *Nat. Genet.* **41**, 415–423 (2009).

12. C. Lefebvre, P. Rajbhandari, M. J. Alvarez, P. Bandaru, W. K. Lim, M. Sato, K. Wang, P. Sumazin, M. Kustagi, B. C. Bisikirska, K. Basso, P. Beltrao, N. Krogan, J. Gautier, R. Dalla-Favera, A. Califano, A human B-cell interactome identifies MYB and FOXM1 as master regulators of proliferation in germinal centers. *Mol. Syst. Biol.* **6**, 377 (2010).

13. X. Zhao, D. D'Arca, W. K. Lim, M. Brahmachary, M. S. Carro, T. Ludwig, C. C. Cardo, F. Guillemot, K. Aldape, A. Califano, A. Iavarone, A. Lasorella, The N-Myc-DLL3 cascade is suppressed by the ubiquitin ligase Huwe1 to inhibit proliferation and promote neurogenesis in the developing brain. *Dev. Cell* **17**, 210–221 (2009).

14. K. Wang, M. Saito, B. C. Bisikirska, M. J. Alvarez, W. K. Lim, P. Rajbhandari, Q. Shen, I. Nemenman, K. Basso, A. A. Margolin, U. Klein, R. Dalla-Favera, A. Califano, Genome-wide identification of post-translational modulators of transcription factor activity in human B cells. *Nat. Biotechnol.* **27**, 829–839 (2009).

15. M. S. Carro, W. K. Lim, M. J. Alvarez, R. J. Bollo, X. Zhao, E. Y. Snyder, E. P. Sulman, S. L. Anne, F. Doetsch, H. Colman, A. Lasorella, K. Aldape, A. Califano, A. Iavarone, The transcriptional network for mesenchymal transformation of brain tumours. *Nature* **463**, 318–325 (2010).

16. S. L. Schreiber, A. F. Shamji, P. A. Clemons, C. Hon, A. N. Koehler, B. Munoz, M. Palmer, A. M. Stern, B. K. Wagner, S. Powers, S. W. Lowe, X. Guo, A. Krasnitz, E. T. Sawey, R. Sordella, L. Stein, L. C. Trotman, A. Califano, R. Dalla-Favera, A. Ferrando, A. Iavarone, L. Pasqualucci, J. Silva, B. R. Stockwell, W. C. Hahn, L. Chin, R. A. DePinho, J. S. Boehm, S. Gopal, A. Huang, D. E. Root, B. A. Weir, D. S. Gerhard, J. C. Zenklusen, M. G. Roth, M. A. White, J. D. Minna, J. B. MacMillan, B. A. Posner; Cancer Target Discovery and Development Network, Towards patient-based cancer therapeutics. *Nat. Biotechnol.* **28**, 904–906 (2010).

CANCER

Survival and Death Signals Can Predict Tumor Response to Therapy After Oncogene Inactivation

Phuoc T. Tran,[1]*[†] Pavan K. Bendapudi,[2]* H. Jill Lin,[3]* Peter Choi,[2] Shan Koh,[2] Joy Chen,[2]
George Horng,[2] Nicholas P. Hughes,[3] Lawrence H. Schwartz,[4] Vincent A. Miller,[5]
Toshiyuki Kawashima,[6] Toshio Kitamura,[6] David Paik,[3‡§] Dean W. Felsher[2‡§]

Cancers can exhibit marked tumor regression after oncogene inhibition through a phenomenon called "onco-gene addiction." The ability to predict when a tumor will exhibit oncogene addiction would be useful in the development of targeted therapeutics. Oncogene addiction is likely the consequence of many cellular programs. However, we reasoned that many of these inputs may converge on aggregate survival and death signals. To test this, we examined conditional transgenic models of K-ras^{G12D}– or MYC-induced lung tumors and lymphoma combined with quantitative imaging and an in situ analysis of biomarkers of proliferation and apoptotic signaling. We then used computational modeling based on ordinary differential equations (ODEs) to show that oncogene addiction could be modeled as differential changes in survival and death intracellular signals. Our mathematical model could be generalized to different imaging methods (computed tomography and bioluminescence imaging), different oncogenes (K-ras^{G12D} and MYC), and several tumor types (lung and lymphoma). Our ODE model could predict the differential dynamics of several putative prosurvival and prodeath signaling factors [phosphorylated extracellular signal–regulated kinase 1 and 2, Akt1, Stat3/5 (signal transducer and activator of transcription 3/5), and p38] that contribute to the aggregate survival and death signals after oncogene inactivation. Furthermore, we could predict the influence of specific genetic lesions ($p53^{-/-}$, Stat3-d358L, and myr-Akt1) on tumor regression after oncogene inactivation. Then, using machine learning based on support vector machine, we applied quantitative imaging methods to human patients to predict both their $EGFR$ genotype and their progression-free survival after treatment with the targeted therapeutic erlotinib. Hence, the consequences of oncogene inactivation can be accurately modeled on the basis of a relatively small number of parameters that may predict when targeted therapeutics will elicit oncogene addiction after oncogene inactivation and hence tumor regression.

INTRODUCTION

Cancer is largely caused by activation of oncogenes or inactivation of tumor suppressor genes, resulting in the pathological disruption of a multitude of cellular signaling programs including cellular proliferation, apoptosis, self-renewal/differentiation, as well as host programs of angiogenesis and immune surveillance (1, 2). Surprisingly, the inactivation of even a single oncogene can induce marked tumor regression, revealing that some tumors can be highly dependent or "addicted" to specific oncogenes (3, 4). Recently, it has been suggested on the basis of in vitro studies in tumor-derived cell lines that such

oncogene addiction may be defined by the interaction between survival and death programs (3, 5, 6). However, these experiments were performed in vitro. It is not clear a priori what factors are most important for determining oncogene addiction. Indeed, several qualitative models for oncogene addiction have been proposed (3, 7, 8).

Evidence for oncogene addiction comes from two sets of observations: work in experimental mouse model systems and in the clinic using targeted therapeutics. Through the use of conditional genetically engineered mouse models, it has been demonstrated that many different tumors exhibit oncogene addiction associated with proliferative arrest, apoptosis, and/or differentiation/senescence (9–15). More recently, it has been suggested that other tumor-intrinsic mechanisms such as the induction of cellular senescence (16) as well as host-dependent programs, including the shutdown of angiogenesis (17), may also be important. The relative contribution of these different cellular programs to the mechanism of oncogene addiction remains to be determined. One possibility is that all of these different cellular programs converge to influence survival and death signals in a cell (3, 5, 6).

The clinical relevance of oncogene addiction became apparent through the discovery of effective clinical therapies that target specific oncogenes. These targeted therapeutics include epidermal growth factor receptor (EGFR) tyrosine kinase inhibitors (TKIs) such as gefitinib and erlotinib for non–small cell lung cancer (NSCLC) (18, 19) and imatinib treatment for chronic myeloid leukemia (20). EGFR mutations are the best predictor of response to EGFR TKIs and improve

the progression-free survival (PFS) of patients with advanced NSCLC who have these *EGFR* mutations (*21–23*).

Methods that could predict the efficacy of targeted therapeutics would be highly useful in the development of new therapies. In addition, because targeted therapies are very expensive (*24*) and are usually only effective to treat a very specific subpopulation of cancer patients, it is important to develop strategies to rapidly discriminate when these agents are effective to help a particular patient. The ideal predictive method would be noninvasive, generate reproducible measurements, and be widely available using technology and clinical skills generally available to most hospitals. Previous efforts to use clinical imaging approaches to predict response to therapy have been limited in their success (*25–30*). It is still not possible to predict with a high degree of certainty by using imaging alone which patients will respond to any particular treatment. Our goal was to develop methods to better predict which patients will respond to oncogene-targeted treatment.

RESULTS

Interrogating oncogene addiction through quantitative imaging and in situ analysis

To gain insight into the mechanism of oncogene addiction and to develop methods that predict when targeted therapies will elicit oncogene addiction, we combined quantitative in vivo imaging with detailed immunohistochemical analysis of conditional transgenic mouse models of lung cancer (*13*) and lymphoma (*9*) (Fig. 1). To analyze our data, we used two complementary mathematical approaches: modeling of the dynamics of cellular survival and death signaling based on ordinary differential equations (ODEs) (Fig. 1A) and prediction of genotype based on a support vector machine (SVM) classifier trained with quantitative imaging data (Fig. 1B).

Cancers that display oncogene addiction are complex and can exhibit the disruption of many cellular programs including cellular
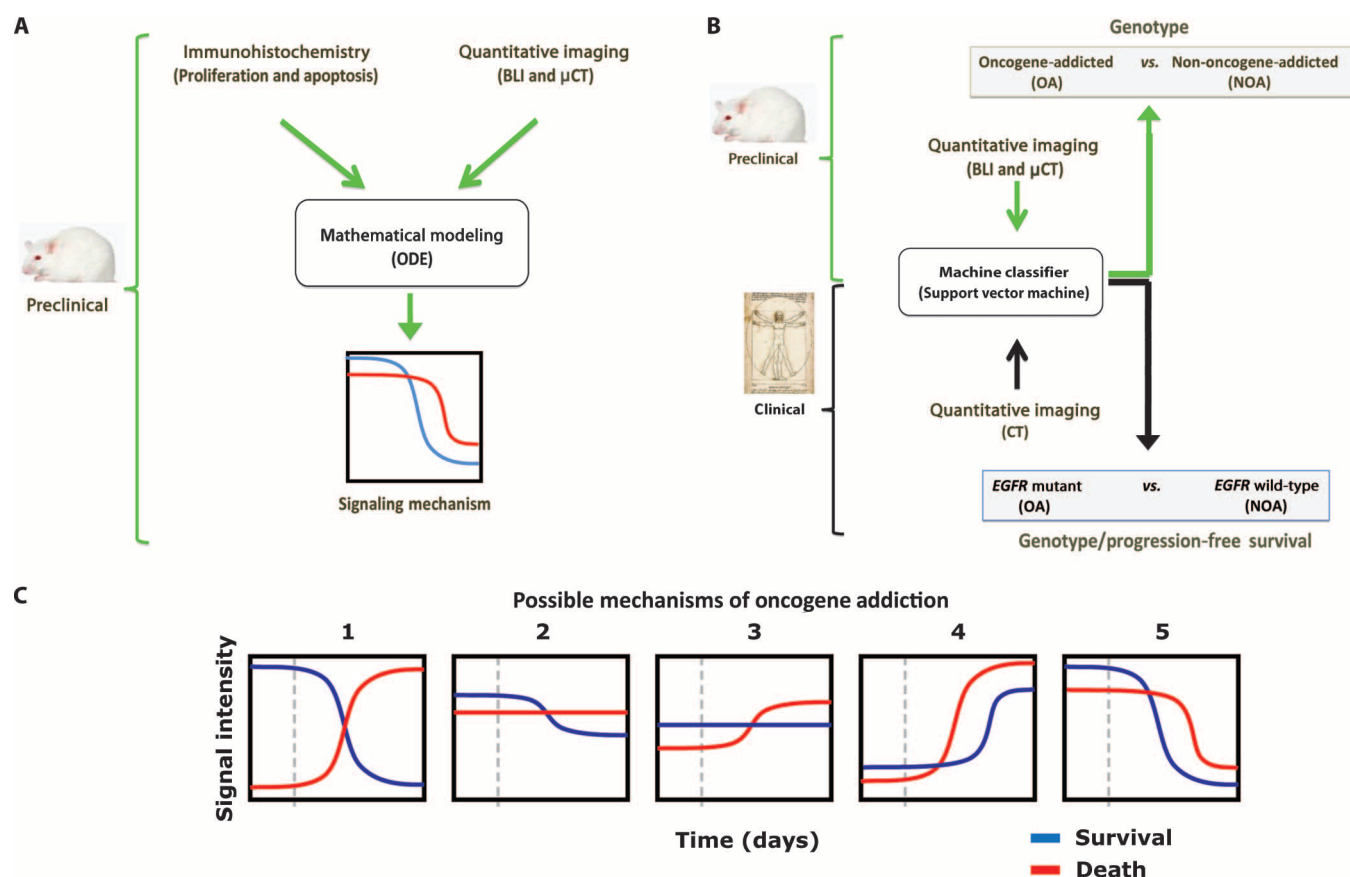

Fig. 1. Multiscale mathematical modeling of oncogene addiction. Two general data sets were considered: preclinical conditional mouse tumor models (green arrows and brackets) and human clinical data (black arrows and brackets). (**A** and **B**) Two complementary mathematical approaches were used (black outlined boxes): (A) ordinary differential equations (ODE) and (B) support vector machine (SVM) classifiers. (A) ODE modeling used immunohistochemistry (IHC) and quantitative imaging data from mice to describe the relationship between aggregate survival and death signaling pathways ("Signaling mechanism") after oncogene inactivation. (B) We used quantitative imaging from mice and humans to predict shortly after oncogene inactivation whether tumors would exhibit oncogene addiction. For humans, we could predict from imaging data alone *EGFR* genotype and longer progression-free survival (PFS). (**C**) Aggregate survival and death signaling behavior after oncogene inactivation. Oncogene-addicted tumor cells may display one of the scenarios upon oncogene inactivation: (1) a reduction in survival signals and an increase in death signals, (2) a reduction in survival signals only without change in death signals, (3) an increase in death signals only without change in survival signals, (4) an increase in survival and death signaling but the latter increasing more, or (5) a decrease in survival and death signaling but with the former decreasing more. The vertical dashed line indicates time at oncogene inactivation.

proliferation, apoptosis, differentiation, and self-renewal, as well as host programs of angiogenesis and immune surveillance (*31*). We reasoned that these programs would both determine tumor formation and predict tumor regression as a consequence of changes in cell survival and cell death signaling (*2*) in several possible ways (Fig. 1C).

To examine these possibilities, we used a transgenic mouse model of *K-ras*^{G12D}–induced lung adenocarcinoma that has been shown to exhibit oncogene addiction. The conditional transgenic model system of *K-ras*^{G12D}–induced lung cancer uses the tetracycline-regulatory ON system (Tet ON), which allows control of target gene expression by the addition or withdrawal of doxycycline in the drinking water of

transgenic mice (Fig. 2A) (*13*). Lung-specific expression of *K-ras*^{G12D} caused multiple primary lung tumors to develop spontaneously in a stochastic manner with moderate latency (Fig. 2, B to E; median latency, 26 weeks). Using the Tet ON system, we could simulate targeted therapy against an oncogene by simply withdrawing doxycycline to turn the oncogene "OFF" (Fig. 2, F to I) (*13, 32*). We measured the kinetics of individual tumor formation and regression in vivo in the transgenic mice by serial weekly microcomputed tomography (μCT) imaging, after activation and then inactivation of *K-ras*^{G12D} (Fig. 2K and fig. S2, A and B). We focused our subsequent analysis on macroscopic tumors that were growing exponentially and therefore by
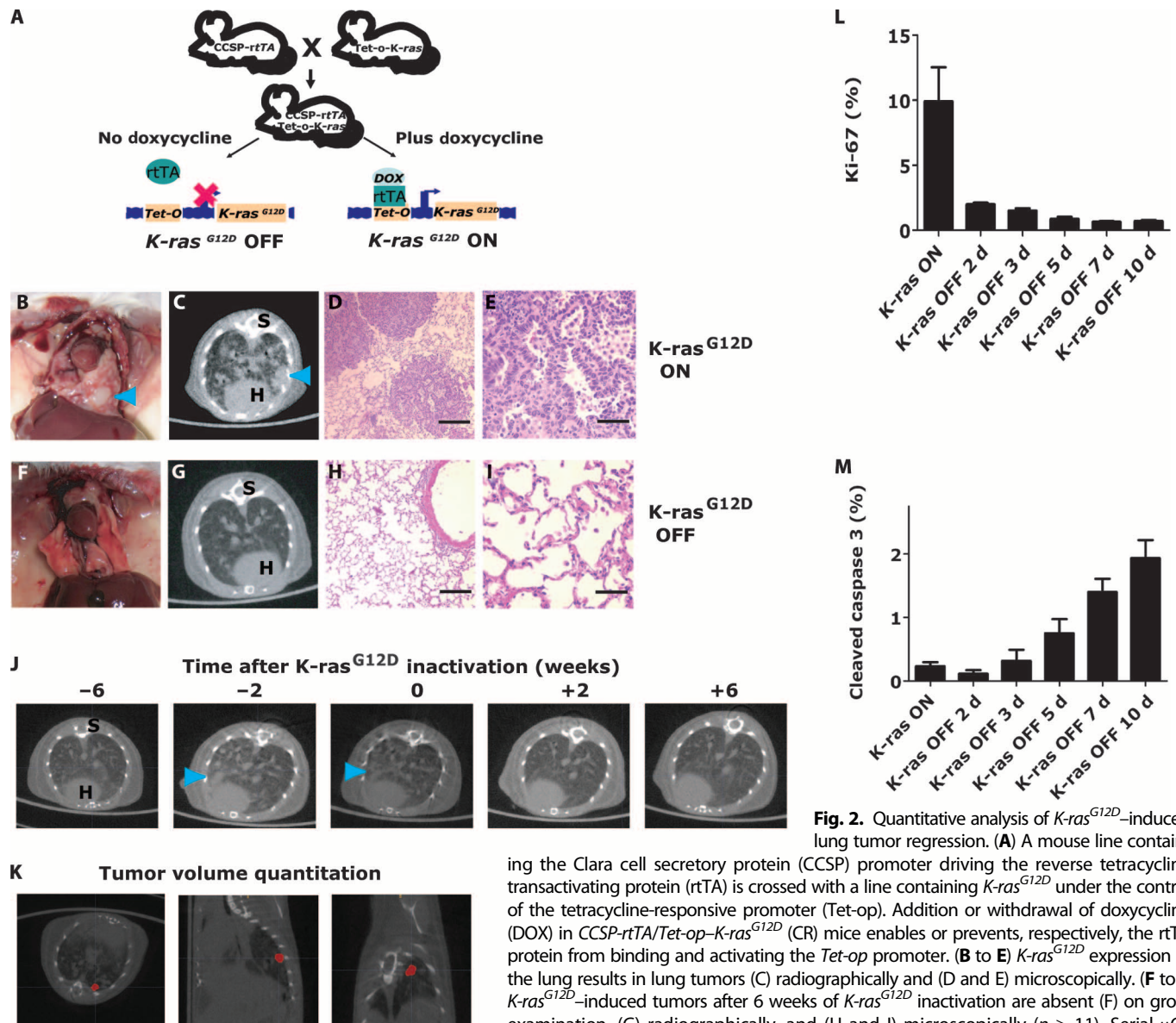
Fig. 2. Quantitative analysis of *K-ras*^{G12D}–induced lung tumor regression. (**A**) A mouse line containing the Clara cell secretory protein (CCSP) promoter driving the reverse tetracycline transactivating protein (rtTA) is crossed with a line containing *K-ras*^{G12D} under the control of the tetracycline-responsive promoter (Tet-op). Addition or withdrawal of doxycycline (DOX) in *CCSP-rtTA/Tet-op–K-ras*^{G12D} (CR) mice enables or prevents, respectively, the rtTA protein from binding and activating the *Tet-op* promoter. (**B to E**) *K-ras*^{G12D} expression in the lung results in lung tumors (C) radiographically and (D and E) microscopically. (**F to I**) *K-ras*^{G12D}–induced tumors after 6 weeks of *K-ras*^{G12D} inactivation are absent (F) on gross examination, (G) radiographically, and (H and I) microscopically (n ≥ 11). Serial μCT representative axial images are shown (C and G). S, spine; H, heart. Tumors are marked by blue arrowheads. Hematoxylin and eosin histology sections show lung tumors or normal lung epithelium (D, E, H, and I). (**J and K**) Tumors were tracked prospectively with serial μCT. Tumor progression and tumor regression after oncogene inactivation were quantified (red pixels) in three dimensions. (**L and M**) Proliferative index (PI) and apoptotic index (AI) in CR lung tumors after turning *K-ras*^{G12D} "OFF" as analyzed by quantization of Ki-67 and cleaved caspase 3 by IHC, respectively. (E, I) Scale bar, 50 μm; (D, H) Scale bar, 200 μm.

definition are adenocarcinomas (*13*, *33*). After oncogene inactivation in this model system, *K-ras*[G12D]–induced lung tumors regress completely within 4 weeks, both radiographically and histologically, as previously described (Fig. 2, F to J, and video S1) (*13*, *32*).

To determine the behavior of prosurvival and prodeath signaling factors after oncogene inactivation in vivo in this transgenic model, we measured over time in lung tumor cells the phosphorylation status of specific prosurvival and prodeath effector molecules by immunohistochemistry (IHC) (Figs. 1A and 3). The primary lung tumor cells demonstrated high steady-state levels of phosphorylated Erk1/2 (extracellular signal–regulated kinase 1 and 2), Akt1, Stat3 (signal transducer and activator of transcription 3), and Stat5 prosurvival effectors before *K-ras*[G12D] oncogene inactivation (Fig. 3, A and B, and fig. S1, A and B, blue outlines or blue bars), as measured by IHC. However, as early as 2 days after oncogene inactivation in the primary lung tumors, these prosurvival molecules were inactive or no longer phosphorylated (Fig. 3, A and B, and fig. S1, A and B). Conversely, the putative prodeath effector p38 (*34*) (Fig. 3, red outline or red bars) was not phosphorylated initially during the *K-ras*[G12D] oncogene inhibition time course (day 0), but phospho-p38 accumulated at day 2, peaked at days 5 to 7, and then eventually decreased in a delayed fashion to a low basal level by day 10 (Fig. 3, A and B). Thus, data from primary lung tumor studies in situ suggested that, after *K-ras*[G12D]

oncogene inactivation, there was a rapid attenuation of prosurvival signaling molecules followed by a burst of prodeath signaling and then a lag or differential attenuation in prodeath mediators.

## Mathematical modeling of oncogene addiction in lung cancer

There are several possible interactions between aggregate survival and death signaling upon oncogene inactivation (Fig. 1C). Our results appeared to be most consistent with two signaling scenarios (Fig. 1C, panels 1 and 5). To distinguish further which scenario was most likely, we generated an ODE model based on the statistical representation of the heterogeneous intracellular signals within different cells across the entire tumor. We modeled tumor growth and regression as being primarily dependent upon a balance of aggregate survival and death signals that could account for temporal patterns in tumor growth before and after *K-ras*[G12D] oncogene inactivation.

Thus, tumor growth is governed by the balance between aggregate survival $[S(t)]$ and death $[D(t)]$ signals. At each time point, cell death and proliferation were simultaneously observed within a tumor, and thus, a deterministic response to a single systemic balance of survival and death signals was insufficient to model the observed response. This heterogeneity of cellular responses was modeled with a normal distribution (log-normal distribution produced virtually identical results) on the difference between survival and death signals, leading to one of three mutually exclusive cellular states: cell proliferation, cell death, or homeostasis/quiescent (Fig. 4, A and B). Two threshold values on the signal difference determined which of the three separate programmed responses was chosen. The homeostatic/quiescent population was defined as noncycling cells and thus may contain cells in G_0, differentiated cells, senescent cells, dormant cells, and/or cancer stem cells. Then, we further developed an ODE to model the change in cell number because of proliferation and apoptosis (Fig. 4C) using logistic functions to represent the time course of aggregate survival and death signals resulting from oncogene inactivation (Fig. 4E).

Proliferation and apoptosis upon oncogene activation and inactivation were characterized by proliferative (PI) and apoptotic (AI) indices via Ki-67 and cleaved caspase 3 IHC. Measurements were made from in situ lung tumor samples at various time points during the first 10 days after oncogene inactivation (Fig. 2, L and M, and fig. S2, C to E). This time period was chosen because it corresponded to the most rapid tumor regression by volumetric analysis from μCT (fig. S2, A and B).

We used the quantitative radiologic and biologic data described above (Fig. 2, K to M, and fig. S2) to estimate parameter values for the ODE model including parameters of the kinetics of aggregate survival and
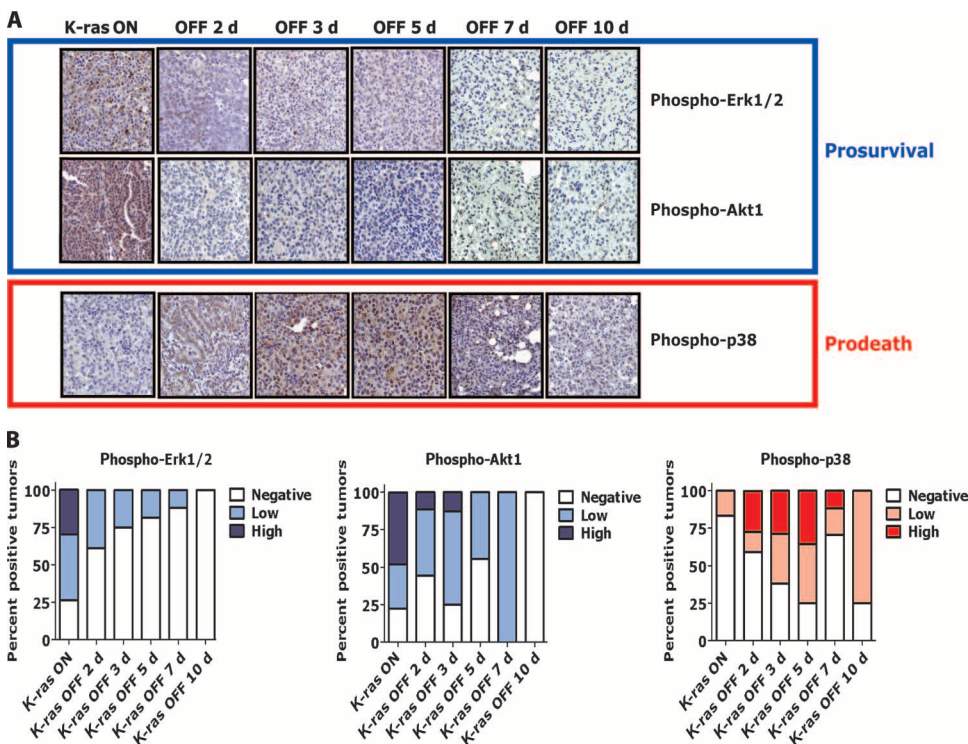
Fig. 3. Differential attenuation of prosurvival and prodeath signaling factors during regression of *K-ras*[G12D]–induced lung tumors in vivo. (**A**) Lung tumors from *CCSP-rtTA/Tet-op–K-ras*[G12D] (CR) mice with *K-ras*[G12D] oncogene activated (or "ON") and at time points after oncogene inactivation (or "OFF") were evaluated for phosphorylation of signaling pathway mediators by IHC. Representative examples show prosurvival pathways mediated by Erk1/2 and Akt1 (blue box) are phosphorylated in lung tumors when *K-ras*[G12D] is ON, but are dephosphorylated after turning *K-ras*[G12D] OFF (days 2 to 3). Prodeath pathway (red box) is dephosphorylated with delayed kinetics (day 10). (**B**) IHC was scored as negative, low (<50% positive cells), or high (>50% positive cells) for tumors.

death signaling, which were not observed directly. The resultant optimization showed an excellent fit with an average percent error within 6.2% [root mean square error (RMSE)] between the model fit and the real data (Fig. 4D and Table 1).
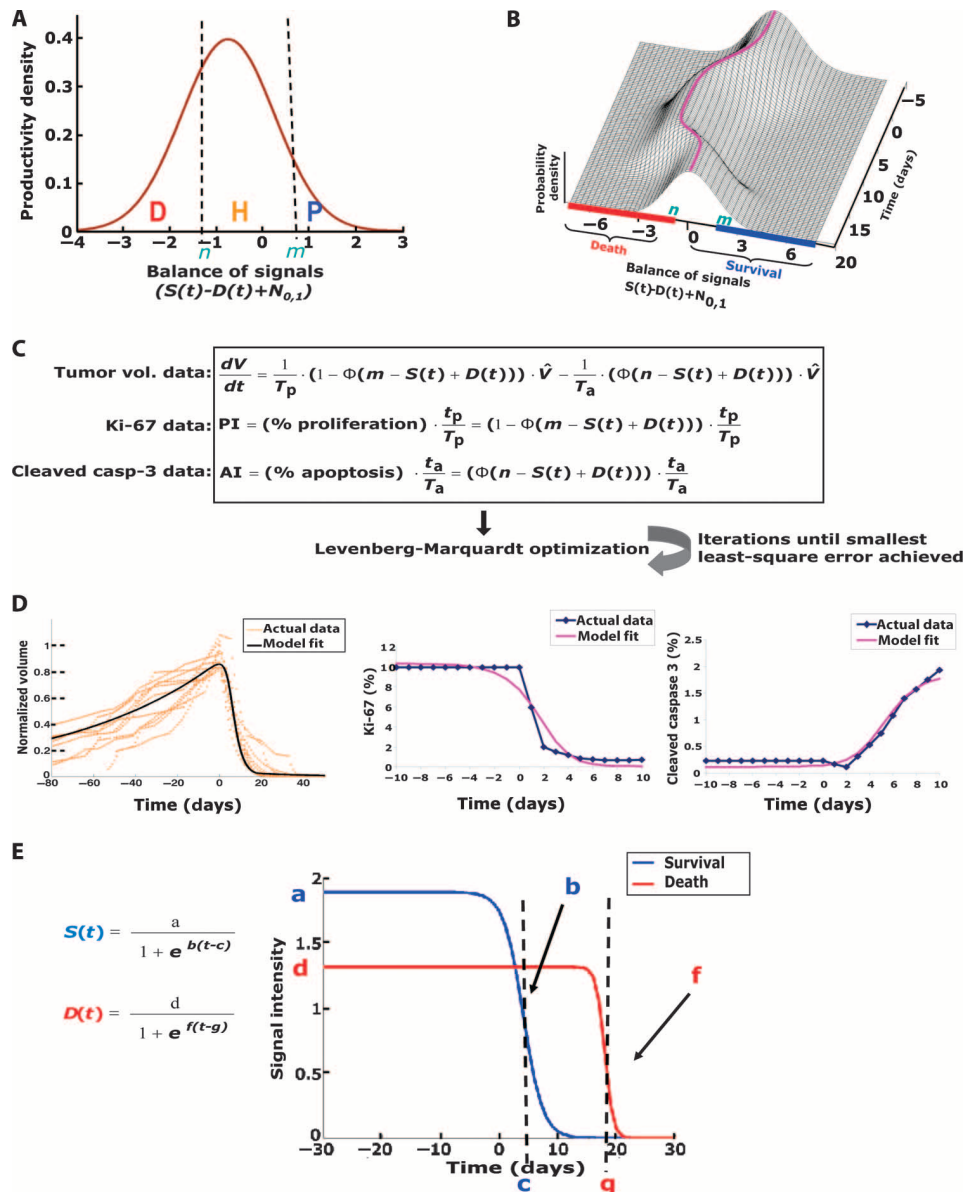
Fig. 4. Mathematical modeling of K-ras^{G12D}–induced lung tumors reveals differential attenuation of survival and death signals. (**A**) Distribution between three cellular decisions directed by the balance of aggregate survival [$S(t)$] and death signals [$D(t)$]. The percentage of cells in each of these states [death (D), homeostasis (H), and proliferation (P)] is determined by thresholds, n and m, and stochastic variability represented by $N_{0,1}$ (standard normal distribution). (**B**) The distribution changes over time with its mean (purple line) centered at $S(t) - D(t)$, shifting the percentage of cells in the three states. (**C**) The first ODE represents changes in tumor cell number because of the increase in cells to the right of threshold m and the decrease in cells to the left of threshold n. Φ is the standard normal cumulative distribution function. The second and third equations represent the PI and AI measured by IHC as a balance of input signals. T_p and T_a are the duration of cell proliferation and apoptosis, respectively. t_p and t_a are the duration of detectability of cell proliferation and apoptosis by IHC, respectively. (**D**) Overall, the model fit well to the original tumor volume data and IHC for PI and AI. (**E**) The logistic functions, $S(t)$ and $D(t)$, and optimized parameters showed that survival signals were short-lived after oncogene inactivation compared to the death signals.

To examine whether our ODE model of aggregate survival and death signals could accurately describe the dynamics observed between intracellular prosurvival and prodeath factors observed in vivo from IHC (Fig. 3), we solved for survival [$S(t)$] and death [$D(t)$] signal intensity and then plotted over time (Fig. 4E). This revealed three marked findings. First, K-ras^{G12D} oncogene addiction could be explained almost entirely by the balance between aggregate survival and death signals as demonstrated by the excellent agreement between the actual radiologic-biologic data (tumor volumes, PI, and AI) and the model-fitted function (Fig. 4D). Second, it surprisingly predicted the almost complete reduction of both aggregate survival and death signaling after oncogene inactivation. Last, there was a notable delay for the final degradation of the death signal compared to the survival signal (Figs. 1C, panel 5, and 4E).

Although the aggregate survival and death signals have yet to be linked with single individual markers, we examined a variety of known prosurvival and prodeath factors by IHC (Fig. 3). The model predicted the initial decline of the aggregate survival signal [$S(t)$] to occur at day 4 after K-ras^{G12D} inactivation (Fig. 4E), similar to what was experimentally observed by days 2 to 3 with the prosurvival factors (Fig. 3, A and B, and fig. S1). Similarly, for the death signal [$D(t)$], the model predicted attenuation of the death signal after K-ras^{G12D} inactivation to begin at day 13, whereas tumors in situ showed decline of the prodeath factor to occur by day 10. Hence, an important implication of the results from our ODE model is that they support the contention that oncogene addiction is a direct consequence of the differential attenuation of aggregate survival and death signals that we observed in vivo (Fig. 1C, panel 5).

Validation of the ODE model

The robustness of the ODE model to different sets of data was validated in several ways. First, we confirmed by a holdout analysis of the model by rotating the removal of one contributing data set from the optimization (tumor volumes, PI, or AI) and then predicting the aggregate survival and death signals. This analysis yielded essentially identical results (fig. S3, A to C) and confirmed that our model was particularly robust. Next, to validate the reproducibility of the ODE model, we performed both bootstrapping (fig. S3D)

Table 1. Multiscale data used to optimize the mathematical model. IHC, immunohistochemistry; IF, immunofluorescence; NA, not applicable; ND, not done.

Data type	K-ras^{G12D}	MYC (lung)	MYC (lymphoma)
Tumor number scored	20	8	21
Cleaved caspase 3 IHC panels scored	24	27	ND
Ki-67 IF panels scored	19	35	ND
μCT volumes scored	202	87	NA
Bioluminescence images scored	NA	NA	70

and sensitivity analysis (fig. S3, E to I), which yielded highly consistent results. Our ODE (Fig. 2C) involved 12 parameters in total (3 survival, 3 death, 4 cell cycle duration, and 2 thresholds) and 245 total observation points (202 μCT scans and 43 IHC panels) (Table 1). All of the statistical validation suggested that the results from our mathematical ODE model were both robust and reproducible.

Next, we tested if our ODE model could generalize to a different transgenic mouse tumor model system and make similar predictions regarding the dynamics of survival and death signals after oncogene inactivation. For this purpose, data were used that involved a different imaging modality [bioluminescence imaging (BLI)] and the examination of a different type of cancer (lymphoma) and measured the response to the inactivation of a different oncogene (MYC) (17). Using the ODE model, as described above (Fig. 4C), modified for optimization with BLI data (fig. S4, C and D; RMSE, 7.0 to 12.6%), we predicted an identical relationship between aggregate survival and death signals between the two different data sets from the transgenic mouse models of lung cancer and lymphoma (compare Figs. 4E and 5, D to F). Thus, our ODE model can be generalized to two imaging modalities: the inactivation of other oncogenes and the examination of different types of cancer.

Impact of genetic changes in survival and death signals of oncogene addiction

Our ODE model predicted that the modulation of aggregate survival and/or death signaling had predictable effects on tumor regression upon oncogene inactivation. To directly test this in our transgenic mouse model of MYC-induced lymphoma, we perturbed the pathways by introducing the constitutively activated forms of Stat3 (Stat3-d358L) (35) and Akt1 (myr-Akt1) (36), and also by looking at the effect of loss of p53 (p53$^{-/-}$) (17), in our model of MYC-induced lymphomagenesis (Fig. 5 and fig. S4). As predicted, the introduction of these mutations into MYC-induced lymphomas had differential effects on apoptosis after MYC inactivation in vitro (fig. S4B).

Next, the in vivo effects of these mutations on the ability of MYC inactivation to induce tumor regression were measured. As predicted from our ODE model, the magnitude of the effect of prosurvival (Stat3-d358L and myr-Akt1) and prodeath (p53$^{-/-}$) pathways on cell death correlated with how quickly tumors regressed after MYC inactivation (Fig. 5). Specifically, Stat3-d358L had no effect on apoptosis (83% apoptotic cells versus 81% for control; P = 0.17 by Mann-Whitney t test; Fig. 5J and fig. S4B) and no effect on tumor regression (Fig. 5A).

Conversely, myr-Akt1 reduced apoptosis modestly (63% apoptotic cells versus 81% for control; P = 0.008 by Mann-Whitney t test; Fig. 5J and fig. S4B) and caused a modest delay in tumor regression (Fig. 5B). Finally, the loss of p53 produced the most marked effect on apoptosis (24% apoptotic cells for p53$^{-/-}$ versus 81% for control; P = 0.0005 by Mann-Whitney t test; Fig. 5J and fig. S4B) and abrogated tumor regression so markedly that tumors were no longer oncogene-addicted (Fig. 5, C and J).

Then, we examined how these mutations resulted in changes in aggregate survival and death signals as predicted by our ODE model (as for Fig. 4). We solved for survival [S(t)] and death [D(t)] signal intensities over time (Fig. 5, G to I, and fig. S4, C to G). As predicted, Stat3-d358L and myr-Akt1 containing lymphomas that behaved in an oncogene-addicted fashion still demonstrated a continuous excess of death signal compared to survival signal during tumor regression (Fig. 5G and H). Furthermore, for myr-Akt1 tumors (Fig. 5J and fig. S4B), the predicted survival signal took longer to decay than control tumors or Stat3-d358L tumors (3 versus 2 days; Fig. 5, D to H). Last, the loss of p53 had the most marked effect on the inhibition of apoptosis (Fig. 5J and fig. S4B), resulting in the absence of tumor regression (Fig. 5C) and the loss of the differential decay between aggregate survival and death signals such that the two signals crossed over each other (Fig. 5I). Hence, our ODE model could predict how changes in survival and death pathways influenced the ability of oncogene inactivation to elicit oncogene addiction.

Recently, MYC inactivation in MYC-induced lung cancers has been shown by us to fail to induce complete tumor regression (32) because of secondary activating events in K-ras and K-ras and associated pathways (32, 37) (fig. S5). We fitted our mathematical model using data from the MYC-induced lung tumors as had been performed for the K-ras^{G12D}–induced lung tumors (Fig. 6A and Table 1). When we solved for aggregate survival [S(t)] and death [D(t)] signals over time, the model fit was very poor (Fig. 6A), thereby demonstrating that our ODE model worked well as predicted on oncogene-addicted tumors but not for non–oncogene-addicted tumors. Thus, when oncogene inactivation is not associated with oncogene addiction, tumor growth kinetics are unable to be explained by differential attenuation of aggregate survival and death signals, as we also observed for the loss of p53 in our model of MYC-induced lymphoma (Fig. 5I).

Prediction of oncogene addiction

We compared the K-ras^{G12D}–induced lung tumor system (oncogene-addicted) (13) to our MYC-induced lung tumor system (non–oncogene-addicted), but because the MYC tumors had tumor signaling dynamics with complexity beyond our ODE model, we used a different approach. We used a machine learning approach, SVM, to determine whether the early tumor growth and regression kinetics alone contain enough information to accurately classify the oncogene-addicted genotype versus non-addicted genotype. The K-ras^{G12D} (fig. S2, A and B) and MYC (fig. S5) μCT-based kinetic regression curves were used to train an SVM algorithm, which is a supervised learning method for classification of data sets (Fig. 7A) (38, 39). Leave-one-out cross-validation was used to estimate the sensitivity, specificity, and overall accuracy of the SVM in classifying oncogene-addicted versus non–oncogene-addicted genotypes (Fig. 7, A and B, and fig. S6A). The SVM was 100% accurate at classifying an oncogene-addicted genotype (K-ras^{G12D}) over a non–oncogene-addicted genotype (MYC) using only the first three serial weekly μCT scans after a simulated
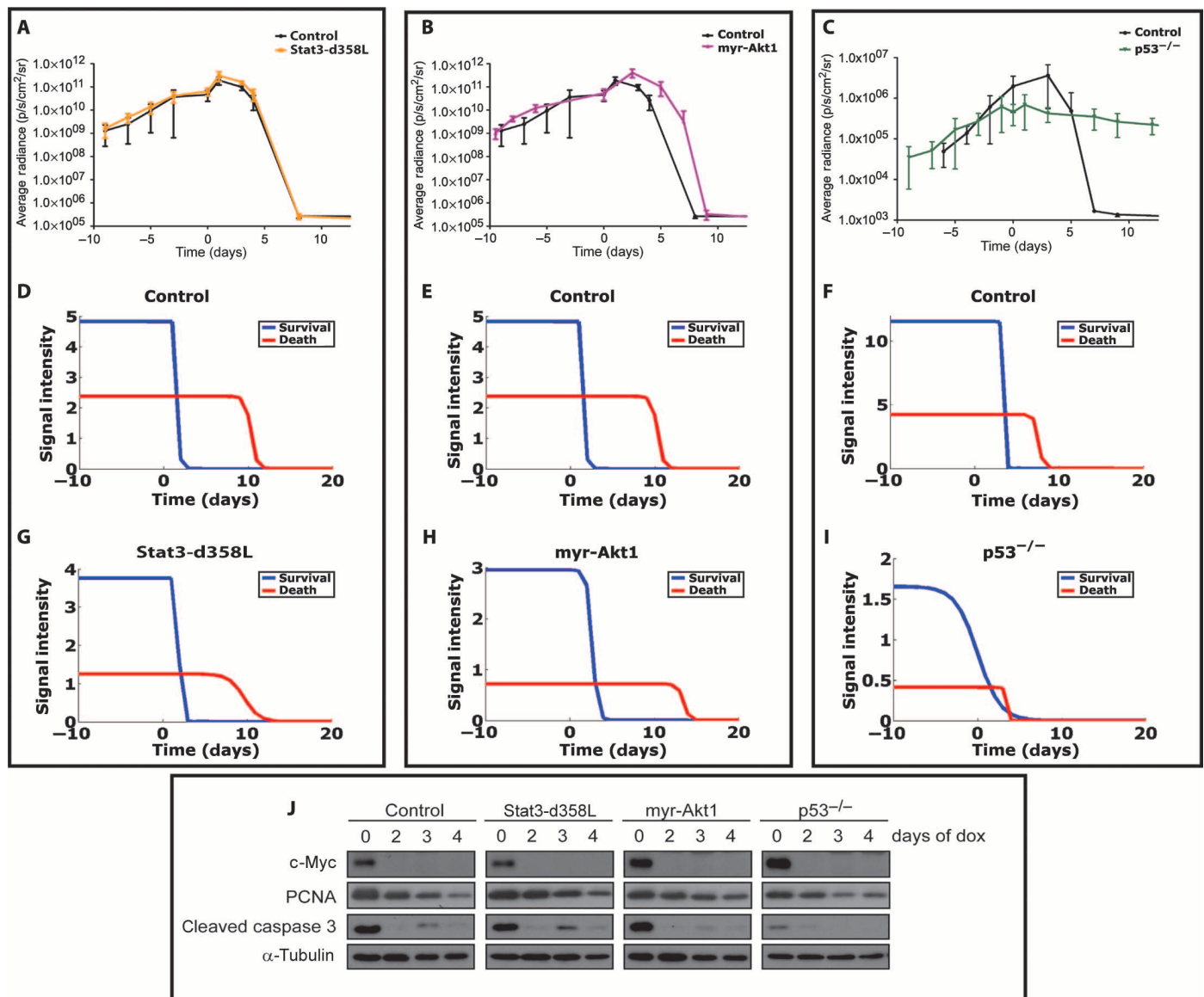
Fig. 5. Mathematical modeling of *MYC*-induced lymphomas with BLI shows that genetic perturbations of aggregate survival and death pathways can impede tumor regression after *MYC* inactivation in vivo. (**A** and **B**) *MYC*-induced lymphomas with control constructs; mutant active forms of (A) Stat3-d358L or (B) myr-Akt1. (**C**) *MYC*-induced lymphoma derived from a p53⁻/⁻ background. *MYC*-induced lymphoma–transplanted tumors were tracked with BLI for growth and regression after *MYC* inactivation (day 0) in vivo (A to C). Resultant BLI data were used to optimize the mathematical model as in Fig. 4, A to C, modified for use with BLI (fig. S4). (**D** to **I**) The survival and death signal plots were then generated from the optimizations for (D to F) control cell lines, (G) Stat3-d358L, (H) myr-Akt1, and (I) p53⁻/⁻ derivative lymphomas. The 6780 *MYC*-induced lymphoma line was used as a control for the p53⁻/⁻ derivative because they had similar basal luciferase activities in vivo. (**J**) *MYC*-induced lymphoma–transplanted tumors with vector control, Stat3-d358L, or myr-Akt1, or isolated from a p53⁻/⁻ background were left untreated or treated with doxycycline (dox) for 2, 3, or 4 days. Samples were harvested at each time point, and lysates were blotted for expression of c-Myc, proliferating cell nuclear antigen (PCNA), cleaved caspase 3, and α-tubulin (loading control).

oncogene-targeted therapy out of 6 to 10 weeks total to train the SVM (fig. S6, B and C).

Then, using imaging data from only the first two weekly scans after oncogene-targeted therapy, the SVM could classify *K-ras*^G12D and *MYC* genotypes with 100% sensitivity and 87.5% specificity (fig. S6, B and C). Even after training the SVM with a more heterogeneous data set where *MYC*- and double *MYC*/*K-ras*^G12D–induced tumors were grouped together (non–*K-ras*^G12D) against *K-ras*^G12D–induced

tumors (Fig. 7B), the SVM was still able to accurately differentiate between *K-ras*^G12D and non–*K-ras*^G12D genotypes (Fig. 7C and fig. S6D). After only 2 weeks of oncogene inactivation, the SVM could classify *K-ras*^G12D versus non–*K-ras*^G12D tumors with 95% sensitivity and 86% specificity. The sensitivity improved to 100% and specificity improved to 93% for *K-ras*^G12D versus non–*K-ras*^G12D tumors, respectively, after 4 weeks of imaging data (fig. S6D). Thus, an SVM classifier tool trained with quantitative CT imaging data can classify oncogene-addicted
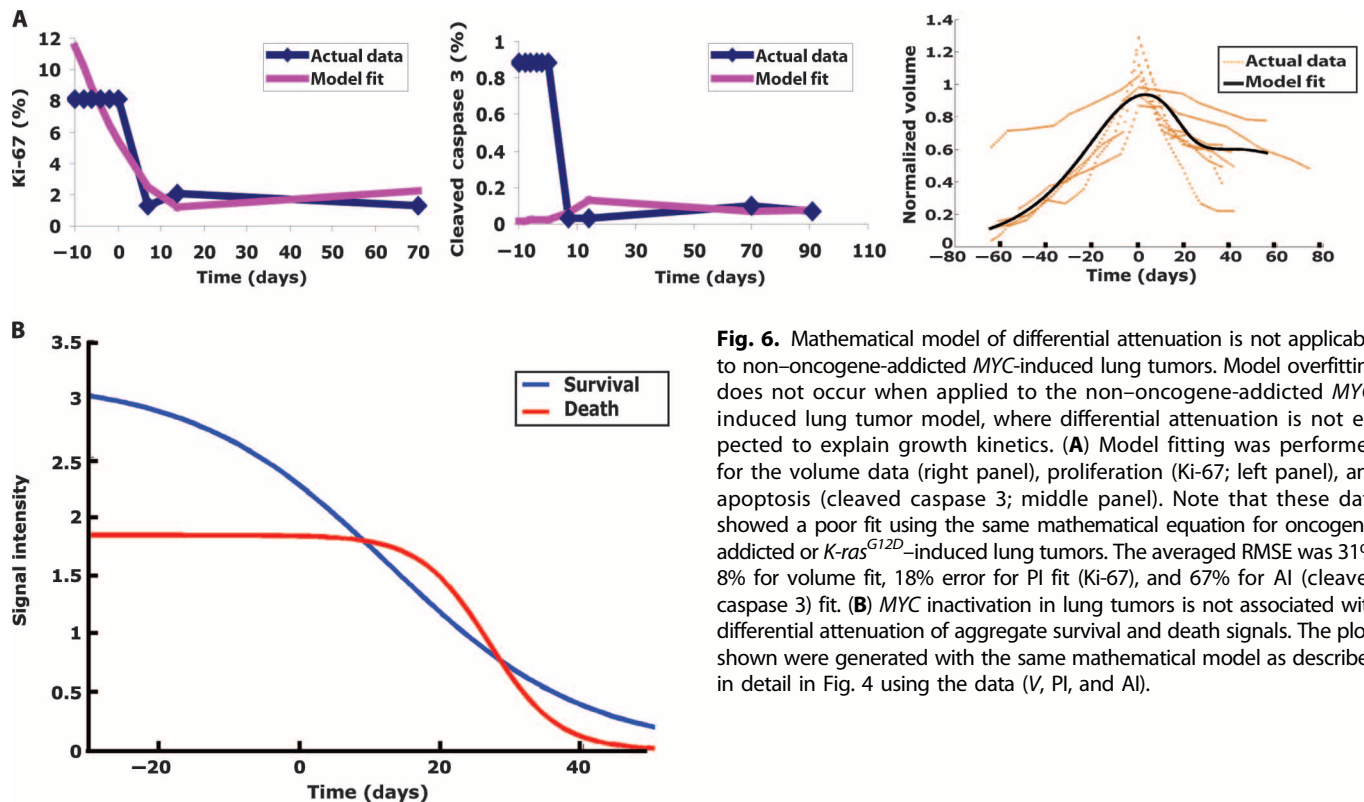
Fig. 6. Mathematical model of differential attenuation is not applicable to non–oncogene-addicted *MYC*-induced lung tumors. Model overfitting does not occur when applied to the non–oncogene-addicted *MYC*-induced lung tumor model, where differential attenuation is not expected to explain growth kinetics. (**A**) Model fitting was performed for the volume data (right panel), proliferation (Ki-67; left panel), and apoptosis (cleaved caspase 3; middle panel). Note that these data showed a poor fit using the same mathematical equation for oncogene-addicted or *K-ras*^G12D^–induced lung tumors. The averaged RMSE was 31%: 8% for volume fit, 18% error for PI fit (Ki-67), and 67% for AI (cleaved caspase 3) fit. (**B**) *MYC* inactivation in lung tumors is not associated with differential attenuation of aggregate survival and death signals. The plots shown were generated with the same mathematical model as described in detail in Fig. 4 using the data (*V*, PI, and AI).

versus non-addicted genotypes and thus predict the tumor response to oncogene inactivation.

Predicting oncogene addiction in human lung cancers

We considered that our SVM approach could be useful to predict in human patients with lung cancer if they will clinically respond to a targeted therapy. To evaluate this possibility, we analyzed patients from a prospective clinical trial who had received the EGFR inhibitor erlotinib for the treatment of lung adenocarcinoma (*40*). *EGFR* mutant lung tumors are reported to behave in an oncogene-addicted fashion after EGFR-targeted therapy, and *EGFR* mutation status is now considered to be the best surrogate for prediction of tumor response and PFS for lung cancer patients undergoing EGFR TKI treatment (*18, 41*).

We quantitatively analyzed CT scan imaging data from the patients for whom the status of *EGFR* mutations was known and for whom paired tumor measurements were available before initiation of erlotinib and then again at the early time point of 4 weeks (*40*). Then, using the SVM classifier generated from the analysis of our transgenic mice as a reference, we correctly assigned the *EGFR* genotype and thus clinical response of 93% of the patients with a positive predictive value of 100% and a negative predictive value of 91% after only 4 weeks of targeted therapy (Fig. 7D). Most importantly, we could predict longer PFS of patients directly from the CT data alone (Fig. 7E; $P = 0.05$, log-rank analysis). Note that from the mouse SVM data, we could predict genotype as early as 2 weeks after targeted therapy (Fig. 7, B and C). We believe that by using our SVM model, we will be able to predict both *EGFR* genotype and PFS earlier than 4 weeks after erlotinib treatment.

DISCUSSION

We have combined direct in vivo analysis of conditional transgenic tumor mouse models and highly quantitative imaging methods to demonstrate that aggregate survival and death signals interact and can be used to predict oncogene addiction. Our results may have important translational implications by enabling one to predict which therapeutics are most likely to elicit oncogene addiction during therapeutic development and therapeutic efficacy in the clinical setting. We show that our ODE model can account for coactivating mutations, including Stat3-d358L, myr-Akt1, and p53^−/−, by modeling their effect on aggregate survival and death signals independently and as a function of time. This provides a possible scalable paradigm to model additional genetic and epigenetic alterations. This could allow early detection of loss of oncogene addiction to allow moving rapidly to alternative therapeutic approaches based on the SVM classification strategy. Finally, we illustrate that quantitative imaging algorithms can be applied to existing CT imaging to assist in the personalized management of lung cancer patients treated with anti-EGFR therapies.

A priori, there were several ways in which aggregate survival and death signaling pathways could behave after oncogene inactivation (Fig. 1C). We developed a quantitative ODE model that could be used to define and predict the behavior of tumor cells upon oncogene inactivation. Using additional quantitative methods that included serial imaging and in situ measurements of proliferation and apoptosis, our ODE model predicted that intracellular aggregate survival signals decay rapidly at a much earlier time point than death signals after targeted therapy. Our ODE model provides a description of the aggregate survival and death signals that would not necessarily be expected by examination of individual
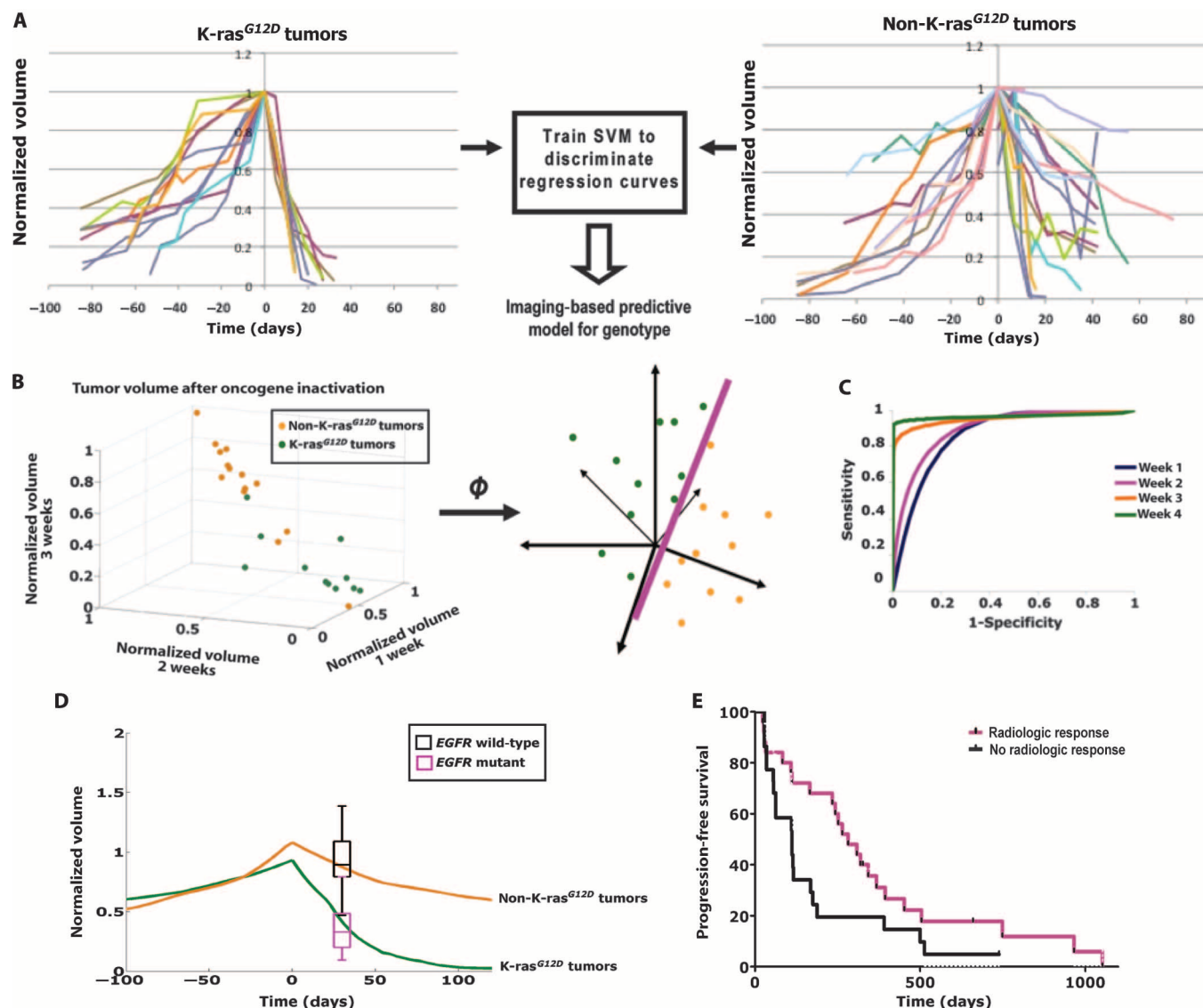
Fig. 7. Modeling imaging data from the regression of human lung tumors treated with targeted therapy can be used to classify genotype. (**A**) Quantitative imaging data after simulated oncogene therapy for *K-ras*^{G12D}– and non–*K-ras*^{G12D}–induced lung tumors are used to train an SVM algorithm. (**B**) An illustration of SVM mapping the original data set in a higher-dimensional space, where a maximal separating hyperplane is constructed that best separates the data points between two different genotypes, *K-ras*^{G12D} and non–*K-ras*^{G12D}, for classification. (**C**) Receiver operating characteristic curves show the accuracy of the SVM technique in predicting the oncogene-dependent genotypes based on tumor volumes obtained from different lengths of time after oncogene-targeted therapy. (**D**) *K-ras*^{G12D} and non–

K-ras^{G12D} tumor volumes over time in orange and green, respectively, scaled for differences between mouse and human tumor doubling times (oncogene inactivation at day 0). The black and cyan box plots with error bars represent tumor responses from patients with *EGFR* mutations (cyan) and wild-type *EGFR* (black) measured 4 weeks after targeted therapy with erlotinib. Mouse *K-ras*^{G12D} and non–*K-ras*^{G12D} tumors behave similarly to human tumors with *EGFR* mutations and wild-type *EGFR*, respectively, after targeted therapy. This model had an 80% (12 of 15) sensitivity and 100% (28 of 28) specificity for assigning *EGFR* mutation status. (**E**) Kaplan-Meier plots of lung cancer patients based on quantitative imaging response at 4 weeks predicted improved PFS ($P = 0.046$).

signaling molecules. Thus, as expected, there are some discrepancies between our ODE model and changes in activation of individual signaling proteins. Initially, after oncogene inactivation, there was no apparent phospho-p38 by IHC staining, but by days 2 to 5 after oncogene inactivation, there was an increase in staining for phospho-p38 (Fig. 3A). It is known that K-ras regulates the prosurvival effector molecules Erk1/2 and Akt1 that in turn negatively regulate p38 phosphorylation status, and thus, we expected low initial phospho-p38 levels (*42–44*).

Our results illustrate that oncogene addiction is associated with a decrease in both aggregate survival and death signaling, but that death signals extinguish more gradually (fig. S7). Our results are consistent but not identical with previous reports based on qualitative in vitro observations in tumor-derived cell lines, which have argued that "differential" attenuation of survival and death signals could account for oncogene addiction (*5, 6*). There are several possible reasons why our results differ slightly from these experiments. The most

obvious is that in contrast to our in vivo study, these previous studies were conducted entirely using cell lines in vitro. However, our modeling is not necessarily mutually exclusive from other proposed models of oncogene addiction (3, 7, 8) that propose mechanisms involving dysregulation of the intracellular signaling or "wiring" in cancer cells (3), oncoprotein-specific negative feedback loops (45), and/or the reconstitution of normal cellular checkpoint programs (7).

We acknowledge that neither our ODE model nor our statistical SVM classifier model incorporates cellular or host programs that are also presumed to be important for tumorigenesis including angiogenesis, genetic instability, or immune function (1). Indeed, our own previous work has specifically identified that angiogenesis and cellular senescence are important mechanisms of oncogene addiction (17, 46). How can we reconcile that a model that incorporates survival and death signals but does not directly include many of these other processes is still capable of describing oncogene addiction? We infer that aggregate survival and death signals may be an integration of many of these other biological programs that ultimately affect proliferation versus cell death, as has been suggested (2, 47). Because our ODE model was generated by analyzing in vivo data, it should incorporate these other biological programs via their effects on survival and death signaling. Indeed, precisely because our analysis was performed with data that were obtained in vivo, our measurements should have incorporated the effects of the tumor microenvironment and we believe accounted for the resulting heterogeneity. Also, although our ODE model does explicitly consider as a possibility that upon oncogene inactivation tumor cells can become homeostatic, which would include cells that differentiate, undergo senescence, or become dormant, none of the conditional mouse tumor models we used in our study displays homeostasis as the primary mechanism for oncogene addiction. Thus, we must consider the possibility that our ODE model may be restricted to tumors that use apoptosis as the primary mechanism for tumor regression after oncogene inactivation. Finally, we recognize that the incorporation of other biological variables is likely to further improve and refine our ODE and SVM classifier models and their predictive potential.

A potential limitation of our study is that we used mouse tumor models that cannot completely recapitulate human disease. However, we have gone to significant efforts to use mouse models that have been shown to approximate closely human tumors. Moreover, mouse K-ras^{G12D}–induced lung tumors behave very similarly after oncogene inactivation (13, 32) or treatment with phosphatidylinositol 3-kinase (PI3K) and mitogen-activated or extracellular signal–regulated protein kinase kinase (MEK) small-molecule inhibitors (15) compared to EGFR-mutated human lung adenocarcinomas after erlotinib treatment (48). Similarly, our transgenic model of lymphoma (9) has been widely used as representative of human MYC-induced T cell acute lymphoblastic leukemia. Therefore, our mouse models appear to be useful to extrapolate tumor behavior that occurs in humans.

Our general approach of using quantitative imaging may be useful to develop new therapeutics as well as to assist in therapeutic decisions for treating cancer patients. Although EGFR mutation status is a strong predictor of therapeutic response and PFS in lung cancer patients treated with anti-EGFR–targeted therapy (18), it is not always possible to sequence EGFR mutations (49). The technology to screen for EGFR mutations is not available in all centers, and performing a biopsy to obtain suitable material may result in increased morbidity to the patient. In contrast, noninvasive quantitative imaging, using struc-

tural [CT or MRI (magnetic resonance imaging)] or functional molecular imaging [PET (positron emission tomography)], can be more widely applied to patients and could be easily translated to most hospitals without the resources of a sophisticated molecular screening core. In general, diagnostic radiologists today evaluate imaging studies such as CT scans in a qualitative fashion; therefore, quantitative algorithms have the capability of performing better and minimizing errors. Automated evaluation of CT scan data after anti-EGFR–targeted therapy for lung cancer has shown some promise. Our results using an SVM classifier trained with quantitative CT imaging data (Fig. 7 and fig. S6) provide a proof of principle that similar approaches may assist in the management of lung cancer patients treated with anti-EGFR therapies and may also help to accelerate the preclinical and clinical validation of other targeted therapeutics. Our preclinical SVM results suggest that it may be possible to identify patients carrying EGFR mutations after as little as 2 weeks of targeted treatment.

Our work demonstrates how transgenic mouse models may be useful to gain insight into the mechanism of oncogene addiction so that it may be possible to more rapidly predict in human patients when targeted therapeutics will be effective. However, we recognize that using additional imaging modalities could further improve upon the results obtained with only structural imaging. Finally, our ability to model accurately the behavior of both lung cancer and lymphoma models suggests that quantitative imaging algorithms, if modified appropriately, could assist in the clinical management of a diverse number of other malignancies.

MATERIALS AND METHODS

Transgenic mice
The TRE-MYC transgenic line generated for these experiments was described previously (9). The CCSP-rtTA and Tet-op–K-ras^{G12D} transgenic lines were provided by J. A. Whitsett (Cincinnati Children's Hospital) and H. Varmus (Memorial Sloan-Kettering Cancer Center, New York), respectively. Mice were mated and screened by polymerase chain reaction (PCR) as below. CCSP-rtTA/TRE-MYC (termed MYC or CM), CCSP-rtTA/Tet-op–K-ras^{G12D} (termed K-ras^{G12D} or CR), and CCSP-rtTA/TRE-MYC/Tet-op–K-ras^{G12D} (termed CMR) expression was activated in the lung lines by administering doxycycline (Sigma) in the drinking water weekly (2 mg/ml) starting at the age of 3 to 4 weeks. All procedures were performed in accordance with Administrative Panel on Laboratory Animal Care protocols, and animals were housed in a pathogen-free environment.

Oncogene inactivation
Transgenic mice were followed by weekly computed tomography scans for a total of >16 weeks. Oncogenes were inactivated in the CM, CR, and CMR cohorts by removing doxycycline from the animals' drinking water before mice became moribund with tumor or when tumors were visualized by μCT.

PCR genotyping
DNA was isolated from mouse tails with the QIAprep DNeasy kit (Qiagen) in accordance with the manufacturer's directions. The CCSP-rtTA segment was detected with the following primers: CCSP-F (5′-ACTGCCCATTGCCCAAACAC-3′) and CCSP-R (5′-AAAATCT-TGCCAGCTTTCCCC-3′) [yielding a 440–base pair (bp) product]. The

TRE-Myc construct was detected with the following primers: Myc-F (5′-TAGTGAACCGTCAGATCGCCTG-3′) and Myc-R (5′-TTTGATGAA-GGTCTCGTCGTCC-3′) (yielding a 450-bp product). Tet-op–K-ras was screened as described previously (*13*). DNA was amplified with the following PCR protocol: 94℃ denaturation for 2 min followed by 35 cycles of 94℃ for 15 s, 59℃ annealing for 30 s, and 72℃ for 30 s, followed by a 5-min extension at 72℃. PCR products were resolved on a 1.5% gel.

Western blot analysis

Western blot analysis was performed with conventional techniques. Tissues or cells were disrupted, and protein was isolated with a tube homogenizer in radioimmunoprecipitation assay lysis buffer. Equal protein was loaded in each lane, as quantified by the BCA (bicinchoninic acid) Protein Assay (Pierce). Proteins were electrophoresed on 8 to 10% tris-HCl polyacrylamide gels at 100 V for 60 min and transferred on polyvinylidene difluoride membranes at 100 V for 60 min. Blotting was then performed as directed by the antibody manufacturer. The following antibodies were used: anti-Stat3 pTyr^{705} (Cell Signaling), anti-Stat3 (Cell Signaling), anti–α-tubulin (Sigma), anti-Akt1 pSer^{473} (Cell Signaling), anti-Akt1 (Cell Signaling), and anti-Erk1/2 pThr^{202}/Tyr^{204} (Cell Signaling).

Apoptosis and proliferation assays

Cells were centrifuged, washed twice with phosphate-buffered saline, fixed in cold 70% ethanol, stained with propidium iodide, and then analyzed with a FACScan flow cytometer for sub-G_1 and S-phase DNA content for apoptotic and proliferative growth fractions, respectively. Alternatively, cells were stained with annexin V–phycoerythrin (BD Pharmingen), and apoptosis was measured by flow cytometry. Data were analyzed with FlowJo (Tree Star Inc.).

Computed tomography

μCT scans were performed on a custom GEHC eXplore RS150 cone beam scanner, which uses a fixed anode with tungsten target source. Animals were anesthetized with 2% isoflurane in a nitrogen/oxygen mixture. Scans were performed at 97-μm resolution with a 70-kV (40 mA) beam to acquire images at 286 radial views over 200° around the subject. Four frames were exposed and averaged in each position. Data were corrected with the GEHC reconstruction utility, and volumes were generated with the same application, which were viewed with the GEHC MicroView software. Mice were exposed to 0.194 Gy (absorbed dose of ionizing radiation) per weekly μCT scan.

Sample population

Weekly μCT scans were collected on 20 *K-ras*^{G12D}–induced mouse lung tumors, 8 *MYC*-induced mouse lung tumors, and 4 CMR-induced lung tumors. Nodular opacities were designated tumors after retrospective review from serial μCT. For the purpose of data analysis, dates of the scans are referred to relative to oncogene inactivation at day 0.

Mathematical modeling of signal behavior

Our mathematical model represents the temporal changes in tumor volumes before and after oncogene inactivation as a balance of two aggregate signals: a survival [$S(t)$] and a death [$D(t)$] signal (*S1*). At any given time, cells may react to the balance of these signals through one of three states: proliferation, homeostasis, or apoptosis. We have defined the homeostatic population of cells as noncycling cells and thus may contain cells in G_0, differentiated cells, or dormant tumor stem cells.

SUPPLEMENTARY MATERIAL

REFERENCES AND NOTES

1. J. Luo, N. L. Solimini, S. J. Elledge, Principles of cancer therapy: Oncogene and non-oncogene addiction. *Cell* **136**, 823–837 (2009).
2. S. W. Lowe, E. Cepero, G. Evan, Intrinsic tumour suppression. *Nature* **432**, 307–315 (2004).
3. I. B. Weinstein, A. Joe, Oncogene addiction. *Cancer Res.* **68**, 3077–3080 (2008).
4. I. B. Weinstein, Cancer. Addiction to oncogenes—The Achilles heal of cancer. *Science* **297**, 63–64 (2002).
5. S. V. Sharma, P. Gajowniczek, I. P. Way, D. Y. Lee, J. Jiang, Y. Yuza, M. Classon, D. A. Haber, J. Settleman, A common signaling cascade may underlie "addiction" to the Src, BCR-ABL, and EGF receptor oncogenes. *Cancer Cell* **10**, 425–435 (2006).
6. W. G. Kaelin Jr., The concept of synthetic lethality in the context of anticancer therapy. *Nat. Rev. Cancer* **5**, 689–698 (2005).
7. D. W. Felsher, Oncogene addiction versus oncogene amnesia: Perhaps more than just a bad habit? *Cancer Res.* **68**, 3081–3086 (2008).
8. S. V. Sharma, J. Settleman, Oncogene addiction: Setting the stage for molecularly targeted cancer therapy. *Genes Dev.* **21**, 3214–3231 (2007).
9. D. W. Felsher, J. M. Bishop, Reversible tumorigenesis by *MYC* in hematopoietic lineages. *Mol. Cell* **4**, 199–207 (1999).
10. M. Jain, C. Arvanitis, K. Chu, W. Dewey, E. Leonhardt, M. Trinh, C. D. Sundberg, J. M. Bishop, D. W. Felsher, Sustained loss of a neoplastic phenotype by brief inactivation of *MYC*. *Science* **297**, 102–104 (2002).
11. C. M. D'Cruz, E. J. Gunther, R. B. Boxer, J. L. Hartman, L. Sintasath, S. E. Moody, J. D. Cox, S. I. Ha, G. K. Belka, A. Golant, R. D. Cardiff, L. A. Chodosh, c-MYC induces mammary tumorigenesis by means of a preferred pathway involving spontaneous *Kras2* mutations. *Nat. Med.* **7**, 235–239 (2001).
12. S. Pelengaris, T. Littlewood, M. Khan, G. Elia, G. Evan, Reversible activation of c-Myc in skin: Induction of a complex neoplastic phenotype by a single oncogenic lesion. *Mol. Cell* **3**, 565–577 (1999).
13. G. H. Fisher, S. L. Wellen, D. Klimstra, J. M. Lenczowski, M. J. Tichelaar, M. J. Lizak, J. A. Whitsett, A. Koretsky, H. E. Varmus, Induction and apoptotic regression of lung adenocarcinomas by regulation of a *K-Ras* transgene in the presence and absence of tumor suppressor genes. *Genes Dev.* **15**, 3249–3262 (2001).
14. H. Ji, Z. Wang, S. A. Perera, D. Li, M. C. Liang, S. Zaghlul, K. McNamara, L. Chen, M. Albert, Y. Sun, R. Al-Hashem, L. R. Chirieac, R. Padera, R. T. Bronson, R. K. Thomas, L. A. Garraway, P. A. Jänne, B. E. Johnson, L. Chin, K. K. Wong, Mutations in BRAF and KRAS converge on activation of the mitogen-activated protein kinase pathway in lung cancer mouse models. *Cancer Res.* **67**, 4933–4939 (2007).
15. J. A. Engelman, L. Chen, X. Tan, K. Crosby, A. R. Guimaraes, R. Upadhyay, M. Maira, K. McNamara, S. A. Perera, Y. Song, L. R. Chirieac, R. Kaur, A. Lightbown, J. Simendinger, T. Li, R. F. Padera, C. García-Echeverría, R. Weissleder, U. Mahmood, L. C. Cantley, K. K. Wong, Effective use of PI3K and MEK inhibitors to treat mutant *Kras* G12D and *PIK3CA* H1047R murine lung cancers. *Nat. Med.* **14**, 1351–1356 (2008).
16. C. H. Wu, D. Sahoo, C. Arvanitis, N. Bradon, D. L. Dill, D. W. Felsher, Combined analysis of murine and human microarrays and ChIP analysis reveals genes associated with the ability of MYC to maintain tumorigenesis. *PLoS Genet.* **4**, e1000090 (2008).
17. S. Giuriato, S. Ryeom, A. C. Fan, P. Bachireddy, R. C. Lynch, M. J. Rioth, J. van Riggelen, A. M. Kopelman, E. Passegué, F. Tang, J. Folkman, D. W. Felsher, Sustained regression of tumors upon MYC inactivation requires p53 or thrombospondin-1 to reverse the angiogenic switch. *Proc. Natl. Acad. Sci. U.S.A.* **103**, 16266–16271 (2006).

18. R. Govindan, INTERESTing biomarker to select IDEAL patients for epidermal growth factor receptor tyrosine kinase inhibitors: Yes, for EGFR mutation analysis, others, I PASS. *J. Clin. Oncol.* **28**, 713–715 (2010).

19. T. S. Mok, Y. L. Wu, S. Thongprasert, C. H. Yang, D. T. Chu, N. Saijo, P. Sunpaweravong, B. Han, B. Margono, Y. Ichinose, Y. Nishiwaki, Y. Ohe, J. J. Yang, B. Chewaskulyong, H. Jiang, E. L. Duffield, C. L. Watkins, A. A. Armour, M. Fukuoka, Gefitinib or carboplatin–paclitaxel in pulmonary adenocarcinoma. *N. Engl. J. Med.* **361**, 947–957 (2009).

20. B. J. Druker, F. Guilhot, S. G. O'Brien, I. Gathmann, H. Kantarjian, N. Gattermann, M. W. Deininger, R. T. Silver, J. M. Goldman, R. M. Stone, F. Cervantes, A. Hochhaus, B. L. Powell, J. L. Gabrilove, P. Rousselot, J. Reiffers, J. J. Cornelissen, T. Hughes, H. Agis, T. Fischer, G. Verhoef, J. Shepherd, G. Saglio, A. Gratwohl, J. L. Nielsen, J. P. Radich, B. Simonsson, K. Taylor, M. Baccarani, C. So, L. Letvak, R. A. Larson; IRIS Investigators, Five-year follow-up of patients receiving imatinib for chronic myeloid leukemia. *N. Engl. J. Med.* **355**, 2408–2417 (2006).

21. W. Pao, V. Miller, M. Zakowski, J. Doherty, K. Politi, I. Sarkaria, B. Singh, R. Heelan, V. Rusch, L. Fulton, E. Mardis, D. Kupfer, R. Wilson, M. Kris, H. Varmus, EGF receptor gene mutations are common in lung cancers from "never smokers" and are associated with sensitivity of tumors to gefitinib and erlotinib. *Proc. Natl. Acad. Sci. U.S.A.* **101**, 13306–13311 (2004).

22. T. J. Lynch, D. W. Bell, R. Sordella, S. Gurubhagavatula, R. A. Okimoto, B. W. Brannigan, P. L. Harris, S. M. Haserlat, J. G. Supko, F. G. Haluska, D. N. Louis, D. C. Christiani, J. Settleman, D. A. Haber, Activating mutations in the epidermal growth factor receptor underlying responsiveness of non–small-cell lung cancer to gefitinib. *N. Engl. J. Med.* **350**, 2129–2139 (2004).

23. J. G. Paez, P. A. Jänne, J. C. Lee, S. Tracy, H. Greulich, S. Gabriel, P. Herman, F. J. Kaye, N. Lindeman, T. J. Boggon, K. Naoki, H. Sasaki, Y. Fujii, M. J. Eck, W. R. Sellers, B. E. Johnson, M. Meyerson, *EGFR* mutations in lung cancer: Correlation with clinical response to gefitinib therapy. *Science* **304**, 1497–1500 (2004).

24. C. A. Uyl-de Groot, G. Giaccone, Health economics: Can we afford an unrestricted use of new biological agents in gastrointestinal oncology? *Curr. Opin. Oncol.* **17**, 392–396 (2005).

25. M. Kartachova, N. van Zandwijk, S. Burgers, H. van Tinteren, M. Verheij, R. A. Valdés Olmos, Prognostic significance of ^{99m}Tc Hynic-rh-annexin V scintigraphy during platinum-based chemotherapy in advanced lung cancer. *J. Clin. Oncol.* **25**, 2534–2539 (2007).

26. M. A. Zahra, K. G. Hollingsworth, E. Sala, D. J. Lomas, L. T. Tan, Dynamic contrast-enhanced MRI as a predictor of tumour response to radiotherapy. *Lancet Oncol.* **8**, 63–74 (2007).

27. M. Schelling, N. Avril, J. Nährig, W. Kuhn, W. Römer, D. Sattler, M. Werner, J. Dose, F. Jänicke, H. Graeff, M. Schwaiger, Positron emission tomography using [^{18}F]fluorodeoxyglucose for monitoring primary chemotherapy in breast cancer. *J. Clin. Oncol.* **18**, 1689–1695 (2000).

28. I. C. Smith, A. E. Welch, A. W. Hutcheon, I. D. Miller, S. Payne, F. Chilcott, S. Waikar, T. Whitaker, A. K. Ah-See, O. Eremin, S. D. Heys, F. J. Gilbert, P. F. Sharp, Positron emission tomography using [^{18}F]-fluorodeoxy-D-glucose to predict the pathologic response of breast cancer to primary chemotherapy. *J. Clin. Oncol.* **18**, 1676–1688 (2000).

29. R. Advani, L. Maeda, P. Lavori, A. Quon, R. Hoppe, S. Breslin, S. A. Rosenberg, S. J. Horning, Impact of positive positron emission tomography on prediction of freedom from progression after Stanford V chemotherapy in Hodgkin's disease. *J. Clin. Oncol.* **25**, 3902–3907 (2007).

30. C. Nahmias, W. T. Hanna, L. M. Wahl, M. J. Long, K. F. Hubner, D. W. Townsend, Time course of early response to chemotherapy in non–small cell lung cancer patients with ^{18}F-FDG PET/CT. *J. Nucl. Med.* **48**, 744–751 (2007).

31. D. W. Felsher, MYC inactivation elicits oncogene addiction through both tumor cell–intrinsic and host-dependent mechanisms. *Genes Cancer* **1**, 597–604 (2010).

32. P. T. Tran, A. C. Fan, P. K. Bendapudi, S. Koh, K. Komatsubara, J. Chen, G. Horng, D. I. Bellovin, S. Giuriato, C. S. Wang, J. A. Whitsett, D. W. Felsher, Combined inactivation of MYC and K-Ras oncogenes reverses tumorigenesis in lung adenocarcinomas and lymphomas. *PLoS One* **3**, e2125 (2008).

33. A. Y. Nikitin, A. Alcaraz, M. R. Anver, R. T. Bronson, R. D. Cardiff, D. Dixon, A. E. Fraire, E. W. Gabrielson, W. T. Gunning, D. C. Haines, M. H. Kaufman, R. I. Linnoila, R. R. Maronpot, A. S. Rabson, R. L. Reddick, S. Rehm, N. Rozengurt, H. M. Schuller, E. N. Shmidt, W. D. Travis, J. M. Ward, T. Jacks, Classification of proliferative pulmonary lesions of the mouse: Recommendations of the mouse models of human cancers consortium. *Cancer Res.* **64**, 2307–2316 (2004).

34. C. Bradham, D. R. McClay, p38 MAPK in development and cancer. *Cell Cycle* **5**, 824–828 (2006).

35. T. Kawashima, Y. C. Bao, Y. Minoshima, Y. Nomura, T. Hatori, T. Hori, T. Fukagawa, T. Fukada, N. Takahashi, T. Nosaka, M. Inoue, T. Sato, M. Kukimoto-Niino, M. Shirouzu, S. Yokoyama, T. Kitamura, A Rac GTPase-activating protein, MgcRacGAP, is a nuclear localizing signal-containing nuclear chaperone in the activation of STAT transcription factors. *Mol. Cell. Biol.* **29**, 1796–1813 (2009).

36. G. Kulik, A. Klippel, M. J. Weber, Antiapoptotic signalling by the insulin-like growth factor I receptor, phosphatidylinositol 3-kinase, and Akt. *Mol. Cell. Biol.* **17**, 1595–1606 (1997).

37. T. D. Allen, C. Q. Zhu, K. D. Jones, N. Yanagawa, M. S. Tsao, J. M. Bishop, Interaction between MYC and MCL1 in the genesis and outcome of non–small-cell lung cancer. *Cancer Res.* **71**, 2212–2221 (2011).

38. W. S. Noble, What is a support vector machine? *Nat. Biotechnol.* **24**, 1565–1567 (2006).

39. M. P. Brown, W. N. Grundy, D. Lin, N. Cristianini, C. W. Sugnet, T. S. Furey, M. Ares Jr., D. Haussler, Knowledge-based analysis of microarray gene expression data by using support vector machines. *Proc. Natl. Acad. Sci. U.S.A.* **97**, 262–267 (2000).

40. V. A. Miller, G. J. Riely, M. F. Zakowski, A. R. Li, J. D. Patel, R. T. Heelan, M. G. Kris, A. B. Sandler, D. P. Carbone, A. Tsao, R. S. Herbst, G. Heller, M. Ladanyi, W. Pao, D. H. Johnson, Molecular characteristics of bronchioloalveolar carcinoma and adenocarcinoma, bronchioloalveolar carcinoma subtype, predict response to erlotinib. *J. Clin. Oncol.* **26**, 1472–1478 (2008).

41. F. Ciardiello, G. Tortora, EGFR antagonists in cancer treatment. *N. Engl. J. Med.* **358**, 1160–1174 (2008).

42. Z. Xia, M. Dickens, J. Raingeaud, R. J. Davis, M. E. Greenberg, Opposing effects of ERK and JNK-p38 MAP kinases on apoptosis. *Science* **270**, 1326–1331 (1995).

43. H. Ichijo, E. Nishida, K. Irie, P. ten Dijke, M. Saitoh, T. Moriguchi, M. Takagi, K. Matsumoto, K. Miyazono, Y. Gotoh, Induction of apoptosis by ASK1, a mammalian MAPKKK that activates SAPK/JNK and p38 signaling pathways. *Science* **275**, 90–94 (1997).

44. A. H. Kim, G. Khursigara, X. Sun, T. F. Franke, M. V. Chao, Akt phosphorylates and negatively regulates apoptosis signal-regulating kinase 1. *Mol. Cell. Biol.* **21**, 893–901 (2001).

45. C. A. Pratilas, B. S. Taylor, Q. Ye, A. Viale, C. Sander, D. B. Solit, N. Rosen, ^{V600E}BRAF is associated with disabled feedback inhibition of RAF–MEK signaling and elevated transcriptional output of the pathway. *Proc. Natl. Acad. Sci. U.S.A.* **106**, 4519–4524 (2009).

46. C. H. Wu, J. van Riggelen, A. Yetil, A. C. Fan, P. Bachireddy, D. W. Felsher, Cellular senescence is an important mechanism of tumor regression upon c-Myc inactivation. *Proc. Natl. Acad. Sci. U.S.A.* **104**, 13028–13033 (2007).

47. S. V. Sharma, M. A. Fischbach, D. A. Haber, J. Settleman, "Oncogenic shock": Explaining oncogene addiction through differential signal attenuation. *Clin. Cancer Res.* **12**, 4392s–4395s (2006).

48. D. T. Milton, G. J. Riely, W. Pao, V. A. Miller, M. G. Kris, R. T. Heelan, Molecular on/off switch. *J. Clin. Oncol.* **24**, 4940–4942 (2006).

49. L. V. Sequist, J. A. Engelman, T. J. Lynch, Toward noninvasive genomic screening of lung cancer patients. *J. Clin. Oncol.* **27**, 2589–2591 (2009).

Supplementary Materials for

Survival and Death Signals Can Predict Tumor Response to Therapy After Oncogene Inactivation

Phuoc T. Tran, Pavan K. Bendapudi, H. Jill Lin, Peter Choi, Shan Koh, Joy Chen, George Horng, Nicholas P. Hughes, Lawrence H. Schwartz, Vincent A. Miller, Toshiyuki Kawashima, Toshio Kitamura, David Paik,* Dean W. Felsher*

*To whom correspondence should be addressed. E-mail: dfelsher@stanford.edu (D.W.F.); david.paik@stanford.edu (D.P.)

This PDF file includes:

Materials and Methods
Fig. S1. Attenuation of prosurvival and prodeath signaling pathway mediators during regression of *K-ras*^{G12D}–induced lung tumors in vivo.
Fig. S2. *K-ras*^{G12D}–induced murine lung tumors are oncogene-dependent.
Fig. S3. Validation of the ODE mathematical model for oncogene-addicted tumor behavior.
Fig. S4. Genetic perturbation of prosurvival and prodeath pathways in *MYC*-induced lymphomas can impede tumor regression after *MYC* inactivation in vivo.
Fig. S5. *MYC*-induced lung tumors are not oncogene-addicted.
Fig. S6. Support vector machine (SVM) trained with quantified imaging data can be used to distinguish *K-ras*^{G12D}– and *MYC*-induced lung tumors.
Fig. S7. Schematic integrating the temporal phospho-IHC in relation to *K-ras*^{G12D} activation state.
References

Other Supplementary Material for this manuscript includes the following:
(available at www.sciencetranslationalmedicine.org/cgi/content/full/3/103/103ra99/DC1)

Video S1 (.avi format). Regression of *K-ras*^{G12D}–induced lung tumors imaged serially using μCT.

Supplementary Material

Materials and Methods

Mathematical Modeling of Signal Behavior. Our mathematical model represents the temporal changes in tumor volumes before and after oncogene inactivation as a balance of two aggregate signals, a survival (*S(t)*) and a death (*D(t)*) signal (*S1*). At any given time cells may react to the balance of these signals through one of three states, proliferation (P), homeostasis (H) or apoptosis (A). We have defined the homeostatic population of cells as non-cycling cells and thus may contain cells in G0, differentiated cells or dormant tumor stem cells:
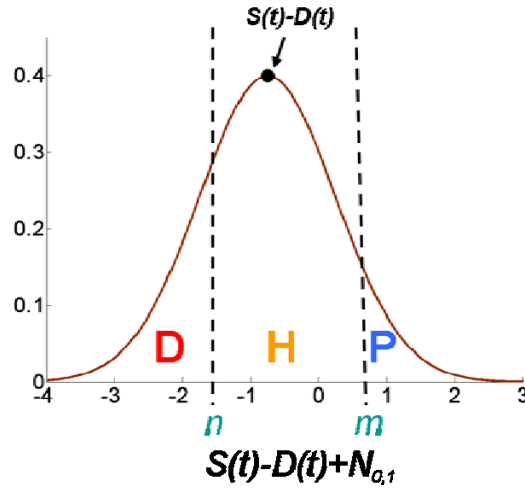
Cells within the same tumor undergo different programmatic decisions as is observed empirically with simultaneous proliferation and apoptosis within a given tumor. The stochastic difference in cell behavior to input signals at the microenvironmental level is modeled using a normal distribution CDF $\Phi(\mu,\sigma^2)$ on the difference between survival and death signals, where μ is the difference between the input signals, and σ is 1. To minimize the number of unknowns and to eliminate a redundant degree of freedom, we fixed the

value σ to 1 and thus, the scale of the signaling intensities is in arbitrary units. Along with

the normal distribution sampling over time (Fig. 4B), the percentage of cells in one of the

three states is also determined by two different thresholds, *m* and *n* (Fig. 4B). We assumed

that the large numbers of cells in the tumor are independent random variables. Based on

the central limit theorem, the re-averaged sum of the large number of random variables will

be approximately distributed normally with finite mean and variance. Therefore, we

assumed normal (or Gaussian) distribution to represent the stochastic difference in cell

behaviors. In addition, the primary determinants of the fate of cells in this mathematical

model are the thresholds *m* and *n*. Therefore, the specific form of distributions used in the

mathematical model should not greatly change the overall prediction.
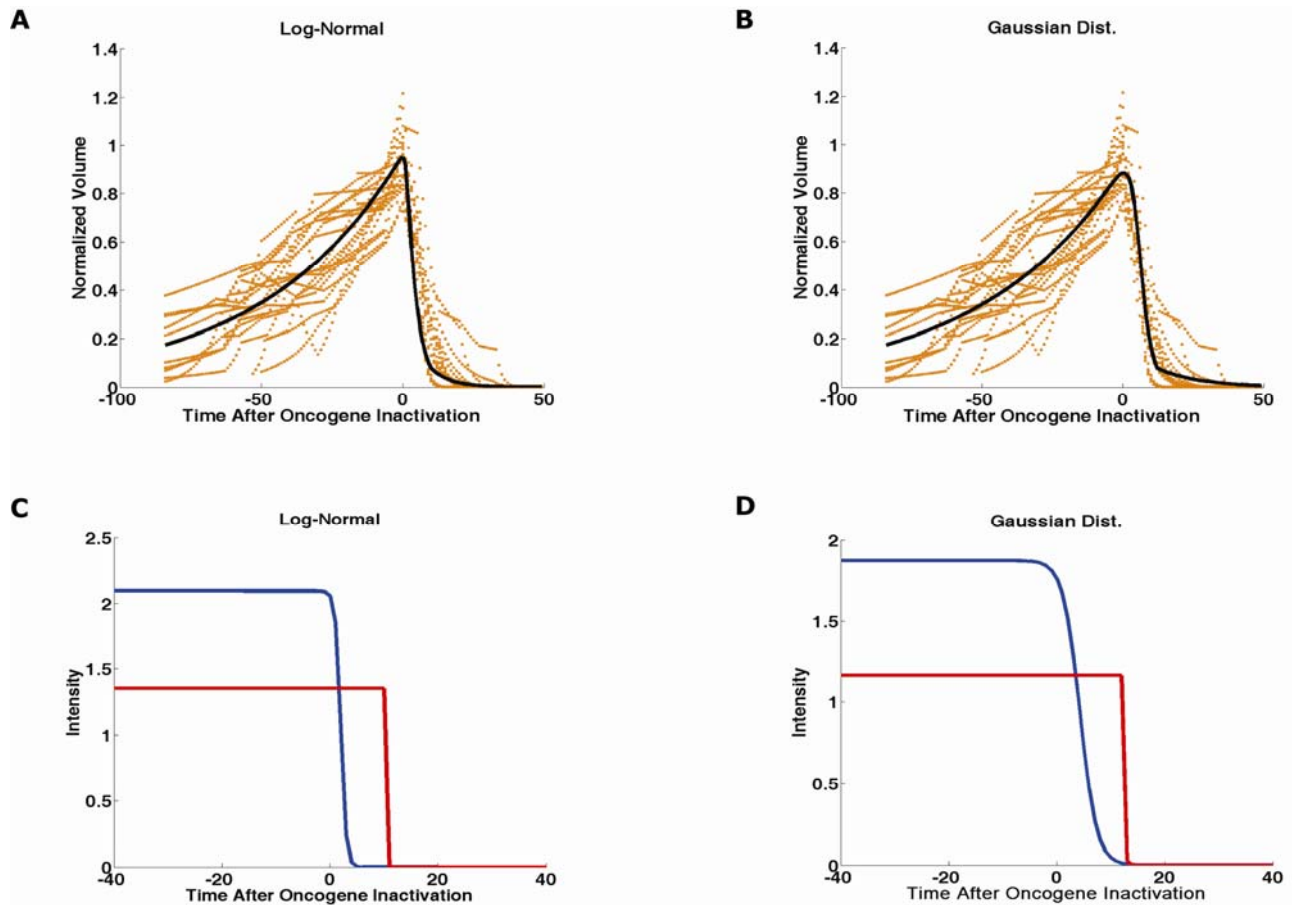
Comparison of the use of normal distribution *versus* log-normal distribution reveals that both functions produce very similar model fit curves for aggregate survival and death signals as shown in the figure above. Regardless of which functions we use to model the behavior of single tumor cells, survival and death signals have similar shapes and decay rates. The model fit well to both of the original tumor volumes using (A) log-normal distribution and (B) normal distribution. The survival signals were short-lived following oncogene inactivation compared to the death signals in both (C) log-normal distribution and (D) normal distribution. The figure above shows that the results generated using normal distribution and log-normal distribution are almost identical. For simplicity, we used normal distribution in the rest of the paper and for setting up the mathematical model.

Therefore, the fraction of cells in each state in response to the balance of the input signals can be summarized as follows,

fraction of cells proliferating $= 1 - \Phi(m - S(t) + D(t))$

fraction of cells in apoptosis $= \Phi(n - S(t) + D(t))$ \hfill (1)

fraction of cells in homeostasis $= 1 - $ (fraction of cells in proliferation) $-$ (fraction of cells in apoptosis)

The rate of volume change over time observed in microCT images is therefore determined by the rates of cell proliferation and cell apoptosis, which are then determined by the balance of input signals. These rates can be determined by dividing the number of cells in each state by the amounts of time required for cell proliferation (T_p) and cell apoptosis (T_a). Therefore, our model to explain the temporal changes over time based on

the balance of the *S(t)* and *D(t)* signals can be mathematically summarized by an ordinary differential equation,

$$\frac{dV}{dt} = \frac{1}{T_p} \cdot (1 - \Phi(m - S(t) + D(t))) \cdot V - \frac{1}{T_a} \cdot (\Phi(n - S(t) + D(t))) \cdot V \qquad (2)$$

The exponential-like individual tumor volume curves were linearly interpolated in semi-log space to minimize interpolation error. Tumors that were too small to be identified on microCT were treated as a single voxel to avoid log(0). In addition, we modeled the behaviors of the survival *S(t)* and death *D(t)* signals as sigmoidal curves because the signals were found to be in a steady state before perturbing the system (inactivation of the oncogene) and we assumed they would reach another steady state some time after perturbation. Therefore, we used the simplest sigmoid function, i.e. the logistic function, commonly used in biological models to represent these intracellular signals which can be mathematically summarized as follows,

$$S(t) = \frac{a}{1 + e^{b(t-c)}}, \quad D(t) = \frac{d}{1 + e^{f(t-g)}} \qquad (3)$$

Parameters *b* and f were the rates of signal decay, *c* and *g* were the amounts of time it takes for the signals to begin dropping off, and *a* and *d* were the starting intensities of the signals. These parameters were estimated using the Levenberg-Marquardt optimization technique (*S2*) to obtain optimal values based on the actual volumetric measurement obtained from microCT images and the IHC data described in the following section.

Equations (4) and (5) also summarizes the temporal rate changes in the IHC data, in particular the measurements of cell apoptosis (represented by cleaved caspase 3 and TUNEL staining) and proliferation (represented by Ki-67). These measurements provide a

measure of cells in a state of proliferation and apoptosis, quantified as an instantaneous percentage. However, in order to quantify the rate as events per unit time, one must also consider the duration for which cells express the markers of proliferation and apoptosis, in this case, t_p for the duration for which casp-3 is expressed and t_a for the duration for which Ki-67 is expressed. For example, a fast rate of events with a shorter duration of detectability could have the same instantaneous percentage as a slower rate of events with a longer duration of detectability (*S3*). Because of a lack of estimates of these durations for these particular tumors in the published literature, we have treated these variables as unknown parameters that are then estimated along with other model parameters. Based on the same assumption for the signaling model, we reasoned that temporal changes in the proliferation and apoptosis rates were also determined by the differences between the survival *S(t)* and death *D(t)* signals. Therefore, the relationship between the signals and the IHC measurements can be mathematically summarized by the following equations:

$$\text{PI} = \textit{(fraction of cells in proliferation)} \cdot \frac{t_p}{T_p} = (1 - \Phi(m - S(t) + D(t))) \cdot \frac{t_p}{T_p} \qquad (4)$$

$$\text{AI} = \textit{(fraction of cells in apoptosis)} \cdot \frac{t_a}{T_a} = (\Phi(n - S(t) + D(t))) \cdot \frac{t_a}{T_a} \qquad (5)$$

where PI is the proliferation index from Ki-67 IHC data, AI is the apoptosis index from cleaved caspase 3 and TUNEL staining IHC data, t_p and t_a were the durations that proliferation and apoptosis, respectively, could be detected by IHC. A couple of assumptions were made in the modeling, 1) PI and AI were at a stable rate before oncogene inactivation, and 2) the asymptotic behavior of PI continued beyond 10 days of oncogene inactivation for *K-ras*[G12D]-induced lung tumors (Fig. 2L). Parameters in

equations (2), (4), and (5) were estimated using the Levenberg-Marquardt (LM) algorithm on combined data of volumetric measurements of microCT images and the Ki-67 and cleaved caspase 3 measurements. The task of the LM algorithm can be stated as follows: given three sets of data points, V_i (normalized volume), P_i (PI) and A_i (AI), determine all parameters $\boldsymbol{\beta}=\{a,b,c,d,f,g,t_a,t_p,T_a,T_p,n,m\}$ of the model curve $f(x,\boldsymbol{\beta})$ to minimize the error function $E(\boldsymbol{\beta})$ in equation 6. $\hat{V}_i(\beta)$, $\hat{P}_i(\beta)$ and $\hat{A}_i(\beta)$ are the fitted values of normalized volume, PI and AI for a given set of parameter values $\boldsymbol{\beta}$. To ensure equal weighting between volume, PI and AI datasets, all three were normalized to their maximum value and mean values were used instead of sums.

$$
\begin{aligned}
E(\beta) = & \sqrt{\frac{1}{n_v}\sum_{i=1}^{n_v}(\hat{V}_i(\beta)-V_i)^2} \\
& + \frac{1}{\max P_i}\sqrt{\frac{1}{n_p}\sum_{i=1}^{n_p}(\hat{P}_i(\beta)-P_i)^2} \\
& + \frac{1}{\max A_i}\sqrt{\frac{1}{n_a}\sum_{i=1}^{n_a}(\hat{A}_i(\beta)-A_i)^2}
\end{aligned}
\tag{6}
$$

Assessment of the Robustness of the Model. To validate our proposed mathematical model, we first performed a hold-out like validation analysis on these datasets, *V, PI* and *AI* in order to ensure that there was no overlap between training and test data. We assumed the duration of cell proliferation and apoptosis, T_a, T_p, detectability of cell proliferation and apoptosis by IHC markers, t_a, t_p, and thresholds that determine cell stochasticity, n, m, remain the same for all oncogene-addicted tumors. We therefore used the values of these parameters from all 20 oncogene-addicted tumors estimated using LM optimization

algorithm and kept them fixed throughout this part of the experiment. Different combinations of two of the three datasets, *{(V,PI), (V,AI), (AI,PI)}*, were used for parameter optimization to assess whether the estimated signal curves would be alike. Each permutation of the hold-out-like validation experiments also resulted in a delayed decay of the aggregate death signal relative to the survival signal (fig. S3A-C).

In addition, we utilized bootstrap statistical method to estimate the sampling distribution and the bias and variance of the optimization algorithm by re-sampling with replacement from the original sample. This is done to validate the robustness of our mathematical model to the data itself using random subsets of the data and to determine the stability of the estimated parameters.

The bootstrap algorithm can be formally described as follows.

For n = 1 to 10,000,

1) For i = 1 to 20,

   a. Randomly select one tumor in the dataset with replacement using uniform distribution.

2) Combine the volume data from the selected tumors with the IHC data to obtain **H**. Repeats in the tumors selected in step 1 are allowed.

3) Estimate all parameters of equation (2) by curve fitting the model with **H** using the LM optimization technique and the objective function described in equation (6).

Finally, to obtain the distribution of each parameter and compute the coefficient of variation (CV) from the bootstrap experiments.

In order to assess the robustness of the proposed method to the values of the estimated parameters from the optimization method, we further performed a sensitivity analysis of each variable. We assessed the average RMSE of the model fit to the actual volume, PI and AI data within the ± 5% of the estimated value. The set of our estimated values for all parameters is considered stable if all values are at the local minimum of the assessed range. Root mean square error (RMSE) for the model fitting of *K-ras*^{G12D} data was 5% error for normalized volume fit, 8.5% error for PI fit (Ki-67), and 5% error for AI fit (cleaved caspase 3) or 6.2% average overall. *MYC* model fit: RMSE was 8% for volume fit, 18% error for PI fit (Ki-67), and 67% for AI (cleaved caspase3) fit or 31% overall.

The fig. S3D-I show the statistics estimated from bootstrap resampling technique and the sensitivity analysis. Both data showed that our mathematical model is robust to variation in the data and to the values estimated from the optimization. Typically, distributions with CV < 1 are considered low-variance, while those with CV > 1 are considered high variance. fig. S3D showed that all parameters are low variance except for the variables that represent the decay rate of aggregate death signal (variable f) and the time when the signal decay is initiated (variable g). In addition, the sensitivity analysis (fig. S3E-I) also demonstrated similar instability in variable g. These observations demonstrated the uncertainty of the duration of the presence of death signal after oncogene inactivation. One possible explanation is that, as tumor volumes become progressively smaller, the limits of the microCT based volumetric measurements become more apparent such that the validity of the absolute time of signal decay is uncertain.

Histology and Immunohistochemistry.

Tissues were fixed in 10% buffered formalin for 24 h and then transferred to 70% ethanol until embedded in paraffin. Tissue sections 5 μm thick were cut from paraffin embedded blocks, placed on glass slides and hematoxylin and eosin (H&E) staining was performed using standard procedures (Stanford Histology Core). We measured Ki67 and TUNEL-staining as described previously (*S4*). Antibodies used in our study: c-Myc (C19) (Santa Cruz Biotech.), cleaved caspase 3 (Cell Signaling Tech.), phospho-AKT-S497 (Cell Signaling Tech.), phospho-Erk1/2-T202/Y204 (Cell Signaling Tech.), phospho-Stat3-Y705 (Cell Signaling Tech.), phospho-p38-T180/Y182 (Cell Signaling Tech.) and phospho-Stat5-Y694 (Cell Signaling Tech.). Samples were dewaxed in xylene and rehydrated in a graded series of ethanols. Antigen retrieval for c-Myc, cleaved caspase 3 and phospho-AKT were performed by 14 min microwave irradiation in citrate-based Antigen Unmasking Solution (Vector Laboratories, Burlingame, CA, USA). Antigen retrieval for phospho-Stat3 and -Stat5 were performed by 14 min microwave irradiation in EDTA, pH 8.0, and antigen retrieval for phospho-Erk1/2 and phospho-p38 was performed by10 min incubation in Pronase (Roche, Basel, Switzerland). Endogenous peroxidases were blocked in either 3% hydrogen peroxide in deionized water (phospho-AKT, -pErk, -p38 and -pStat3/5) or 0.3% hydrogen peroxide in methanol (c-Myc and cleaved caspase 3) for 10-20 minutes. Non-specific binding was blocked with 5 -10% goat serum for 60 minutes. Primary antibodies were used at appropriate dilutions (c-Myc, phospho-AKT, -pErk and -p38 at 1:100; cleaved caspase 3 at 1:150; phospho-Stat5 at 1:200; and phospho-Stat3 at 1:50) and sections

incubated overnight at 4 degrees Celsius. Detection was conducted using the Vector Elite

ABC detection kit (Vector Laboratories) with 3,3'-diaminobenzidine tetrahydrochloride as

the chromogen. Sections were counterstained with Gill's hematoxylin (Vector

Laboratories).

Tumor Segmentation.

A semi-automated open source image analysis application, ITK-Snap (*S5*), was

employed for segmentation of the lung tumors from the microCT images. The tool uses a

level set algorithm to semi-automatically delineate tumor from background by expanding a

level set from a user-defined seed point. We viewed 2D images in sagittal, coronal and

transverse views to detect tumors and track them over time. The segmentation algorithm

was seeded manually and stopped once the tumor boundary was detected. The post-

processing of the segmented data provided the voxel counts, the volume (in cubic

millimeters) and displayed the shape of the segmented structure. Matching tumors across

time points was performed manually by simultaneous viewing of the serial data. This

volume information was then used for analysis of the temporal changes in lung tumor

nodules. MicroCT imaging has been shown to correlate with the number and volume of

murine lung tumors found on necropsy (*S6*).

Normalization.

Peak tumor volumes at the time of oncogene inactivation had significant variability

due to the subjective determination of when the oncogene was inactivated and also due to

the variability in tumor sizes in the same mouse. However, simple normalization by peak

tumor volume was artificially biased toward a single time point due to zero variance at time zero (peak) and exaggerated variance at large negative and positive times. Instead, we weighted each time point equally in the normalization process. Due to the exponential-like growth and regression pattern observed in volume data, two straight lines were fitted by least squares to tumor volume in semi-log space, one for the growth phase and one for the regression phase. The value at the intersection of the two straight lines was then used to normalize the volume for each tumor time series (fig. S2A). Normalized tumor volumes at each scan time were averaged across all tumors to obtain a general trend of the growth and regression patterns leading to much more consistent variance in tumor volume measurements across time.

MYC-induced Lymphoma Mouse System.

MYC-induced lymphoma cells expressing luciferase were transduced using retrovirus carrying either pBabe-puro, pMx-Stat3d358L-puro, or pBabe-MyrAktHA-puro. Infected cells were then selected with 1 μg/ml puromycin. Ten million MYC-induced lymphoma cells were injected subcutaneously and then were scanned every 2-5 days prior to oncogene inactivation and 20 days after oncogene inactivation using BLI imaging (*S7*). Average radiance (p/s/cm2/sr) of each scan was collected and treated similarly as volumetric measurements for the $K\text{-}ras^{G12D}$–induced lung tumors and was used to study tumor kinetics. A similar normalization method was used on the BLI measurements. We fitted the BLI data to equation (2) to obtain the necessary parameters for estimation of *S(t)* and *D(t)* behaviors.

Support Vector Machine (SVM) Classification.

v-SVM and leave-one-out techniques were used for the classification and prediction

of tumor genotype based on the first few serial weekly scans after oncogene inactivation. A

recent paper by Basavanhally *et. al.* (S8) has shown that for various medical image

classification tasks, SVM has best performance (compared to kNN and C4.5) for n>13

training set size. Our data set was n~20 for the SVM. Although the datasets and tasks

differ, we believe this indicates that SVM is a reasonable choice of classifier. Two classes

of data points were constructed: (1) 20 *K-ras*^{G12D} oncogene-induced tumors, and (2) 8 non-

oncogene addicted *MYC*-induced mouse tumors also following simulated *MYC* oncogene

targeted treatment. v-SVM algorithm can be summarized as follows. Given a dataset D of

n samples, $(S_1,L_1),\cdots,(S_n,L_n)$, where $S_i = <s_1,s_2,\cdots,s_m>$ was a set of feature vectors which in

our case were the tumor volumes from weekly scan, and $L_i \in \{-1,+1\}$ represented the binary

class membership, SVMs mapped the input data into a high-dimensional feature space, and

constructed a maximum margin hyperplane to separate the two classes in order to predict

the label of a new sample. In this work, we used the Gaussian kernel

$$k(S,S') = \exp(-d(S,S')^2)/\sigma^2)$$ to map the input data to the high-dimensional feature

space, where *S, S'* were two feature vectors, d was the Euclidean distance, and σ the width

parameter of the kernel. We selected the width σ of the kernel by minimizing the leave-

one-out error estimate of the classification error between the true label and the predicted

value of the v-SVM classification function for each σ. In our experiments simulating a

more heterogeneous population, we included 20 oncogene addicted *K-ras*^{G12D} tumors, 8

non-oncogene addicted *MYC* tumors and 6 double mutant, *MYC*/ *K-ras*^{G12D}, tumors for training and classification. Training data was derived from normalized tumors volumes.

Mouse and Human Lung Tumor Regression Analysis.

Human lung tumor measurements from CT scan data were performed according to the World Health Organization (WHO) standards. Bi-dimensional tumor measurements were performed before and 4 weeks following erlotinib therapy by obtaining the longest diameter of the tumor in the axial plane and the greatest perpendicular to it. Tumor volume was calculated as a sphere and percent change at follow up was calculated as a percentage of baseline value. The median doubling time of human lung tumors is 144 days (S9-S11) while the conditional transgenic mouse lung tumors in our study double every 37.04 days. To correct for different growth kinetics between species, mouse tumor kinetics were expanded by a factor of 3.89 (human tumor doubling time divided by mouse tumor doubling time). Using this analysis, at one month after oncogene inactivation, the average change in volume of oncogene addicted mouse lung tumors (*K-ras*^{G12D}) was 58.5% while patients with *EGFR* mutations had average change in tumor volume of 60.9%. Similarly, the average change in volume of non-oncogene addicted mouse lung tumors (non-*K-ras*^{G12D}) was 12.5% while patients with wildtype *EGFR* had an average change of 5.7%.

Supplementary Figures

Fig. S1

A
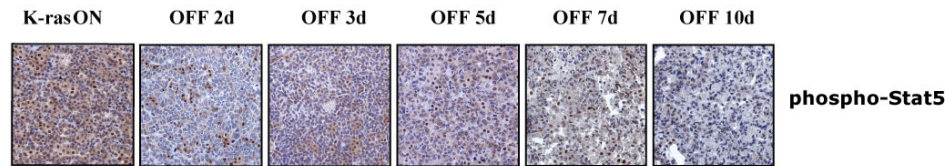
B
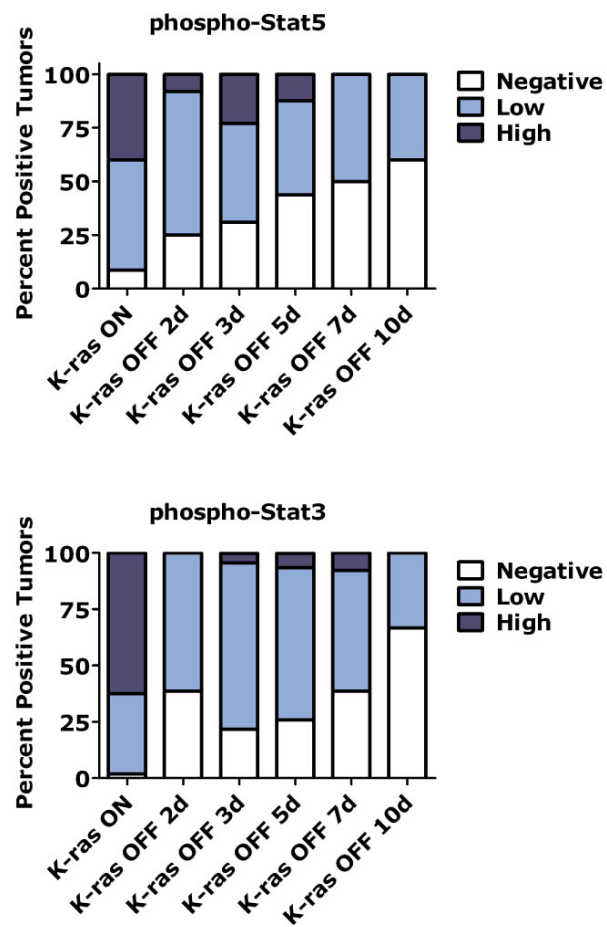
Fig. S1. Attenuation of prosurvival and prodeath signaling pathway mediators during

regression of *K-ras*[G12D] –induced lung tumors in vivo. (A) *K-ras*[G12D] induced lung tumors with

K-ras^*G12D* oncogene activated (or "ON") and at time points following oncogene inactivation (or "OFF") were evaluated for phosphorylation of signaling pathway mediators by IHC. Representative examples show prosurvival pathways mediated by STAT5 are phosphorylated in lung tumors when *K-ras*^*G12D* is "ON," but are de-phosphorylated after turning *K-ras*^*G12D* "OFF" (day 2-3). (B) Phospho-Stat5 and –Stat3 IHC was scored using similar system as in Fig. 3B.

Fig. S2

A

B
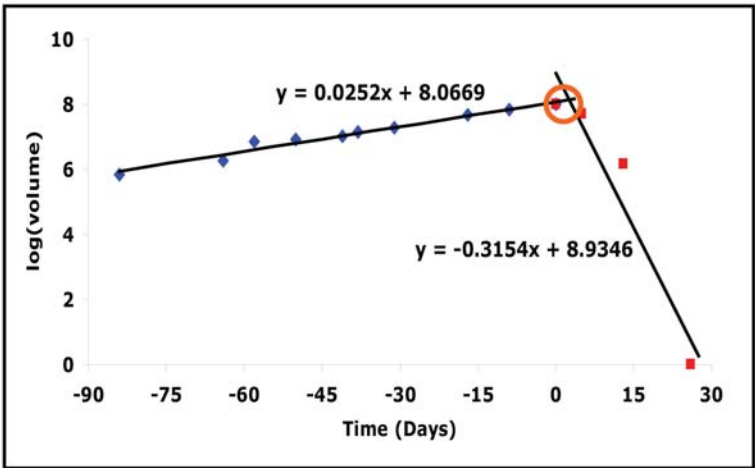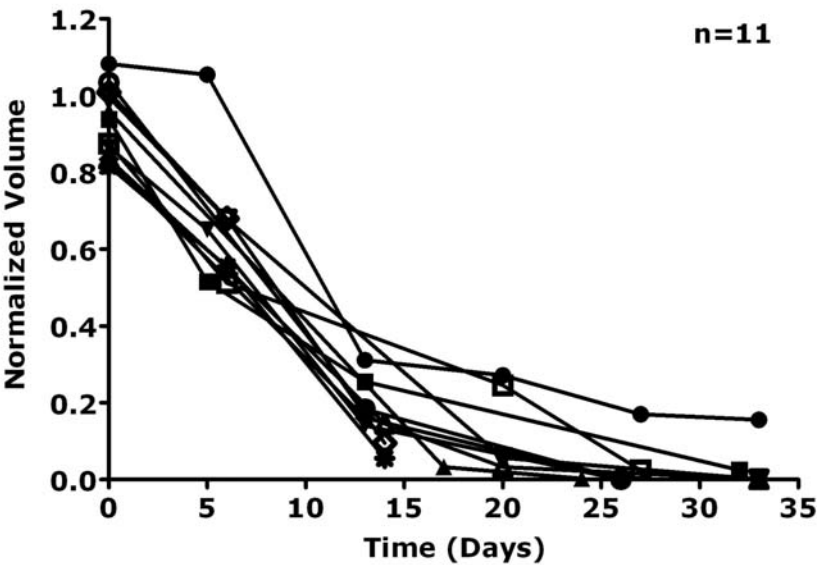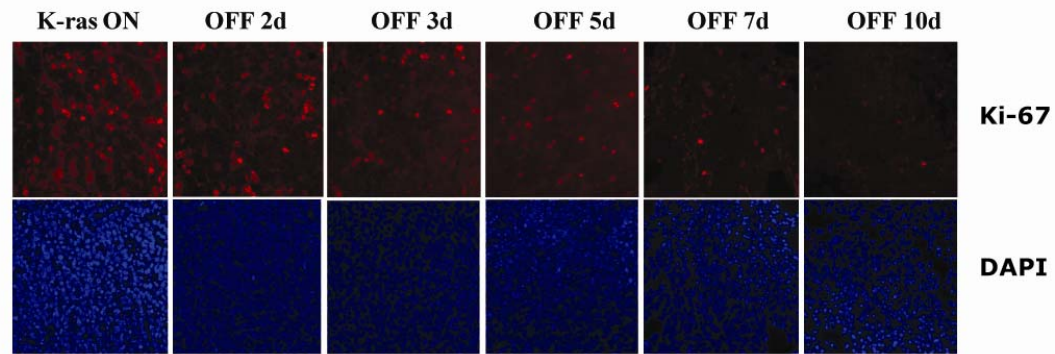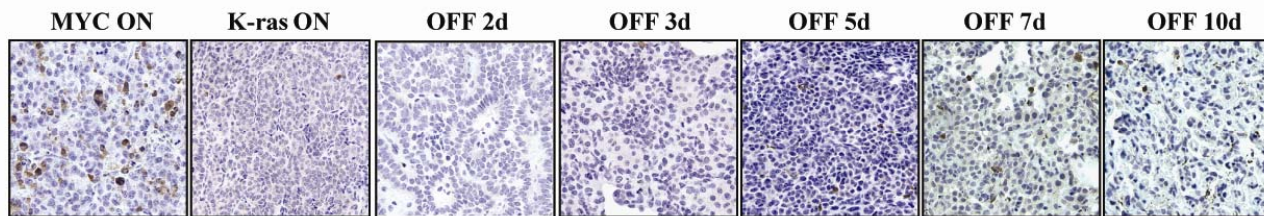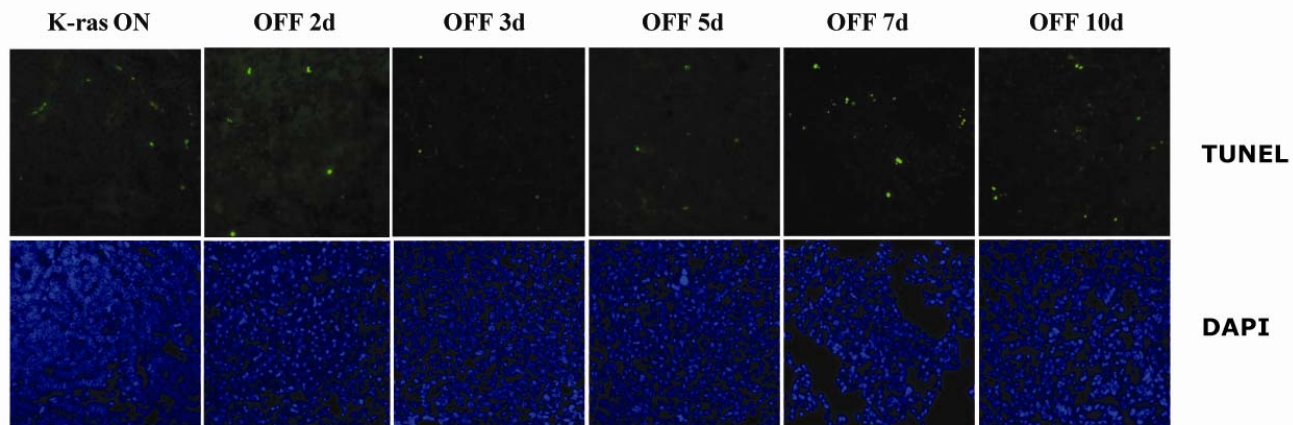
Fig. S2. *K-ras^{G12D}* -induced murine lung tumors are oncogene-dependent. (A) Volumetric quantization of *K-ras^{G12D}* lung tumors using serial microCT. Representative tumor volume plotted as two straight lines fitted by least squares in semi-log space, one for the growth phase and one for the regression phase. (B) Oncogene inactivation in *K-ras^{G12D}* lung mice show individual lung tumors quantified and normalized over time as described in Supporting Materials and Methods show consistent complete regression of CR lung tumors (n=11). (C) Sections of *K-ras^{G12D}*–induced lung tumors following doxycycline withdrawal time course show decreasing proliferation with time as demonstrated by immunofluorescence (IF) against Ki-67. (D & E) Increased frequency of apoptotic cells with time after switching *K-ras^{G12D}* "OFF." (D) Similar CR lung tumor sections were stained for cleaved caspase 3 and showed increased apoptosis after switching *K-ras^{G12D}* "OFF." (E) Lung tumor samples were assayed for apoptotic cells using the TUNEL procedure and imaged using IF at the indicated time points relative to switching *K-ras^{G12D}* "OFF". IF sections were counterstained with DAPI to indicate cell number.

Fig. S3

A. Predicting proliferation index and signal curves using apoptosis index and volume
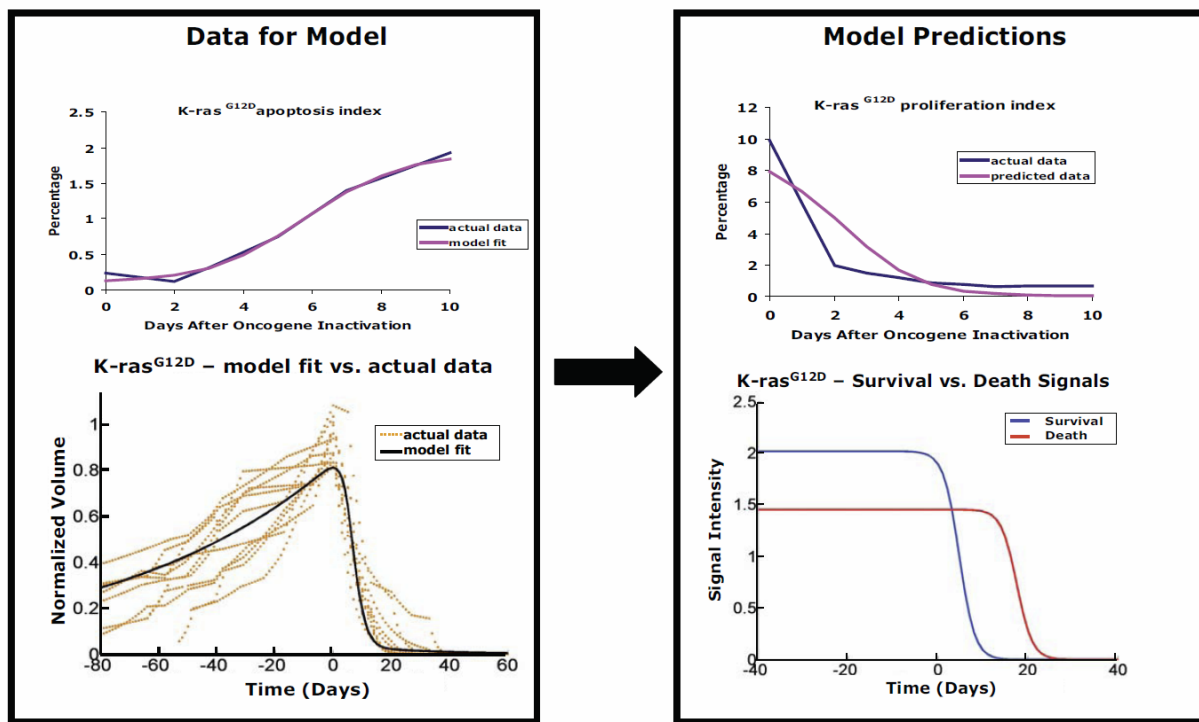
B. Predicting apoptosis index and signal curves using proliferation index and volume data
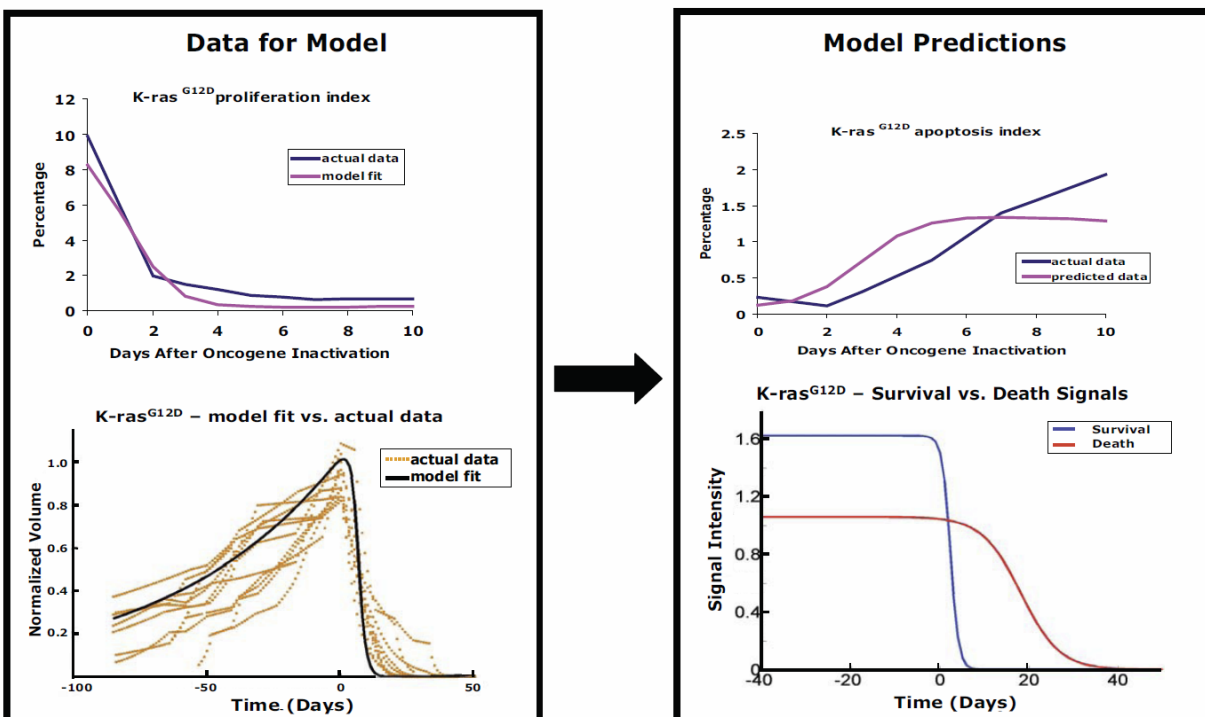
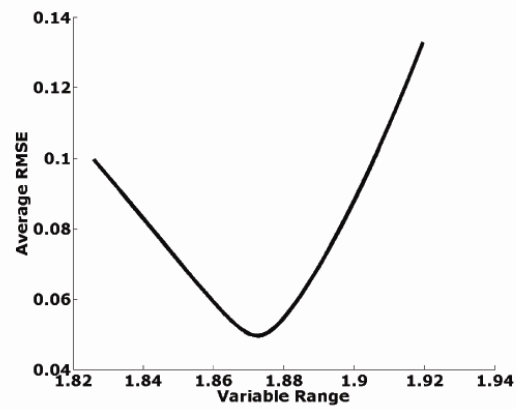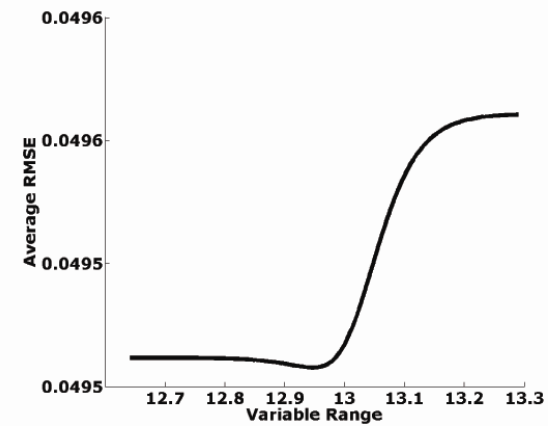## C. Predicting volume data and signal curves using proliferation and apoptosis indices

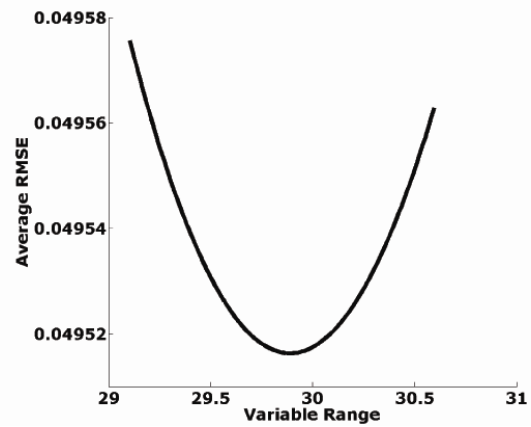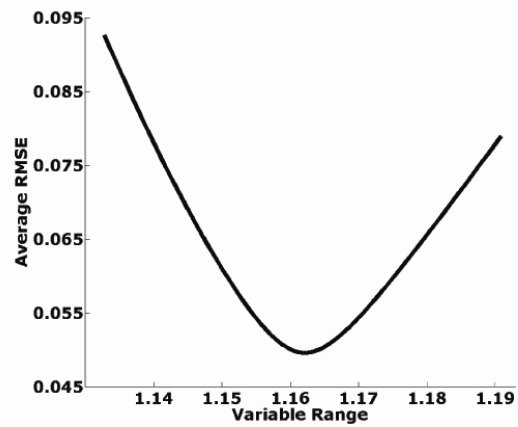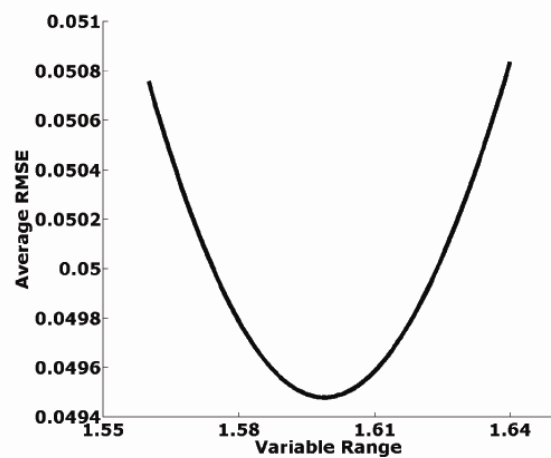**Data for Model**

K-ras^{G12D} proliferation index

K-ras^{G12D} apoptosis index

Model Predictions

K-ras^{G12D} – model fit vs. actual data

K-ras^{G12D} – Survival vs. Death Signals
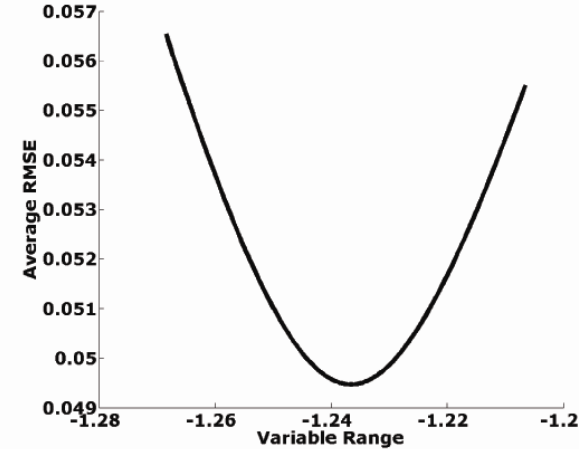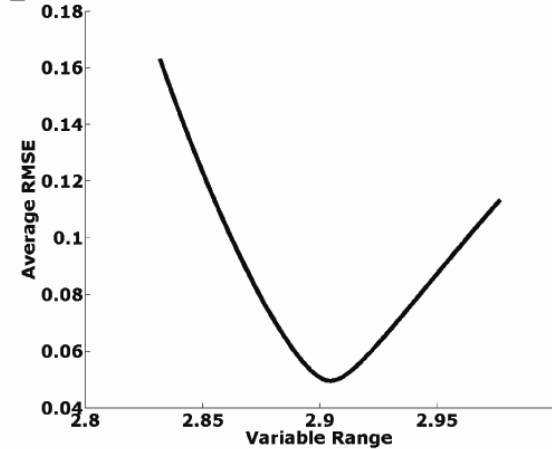
D

Bootstrapping Results
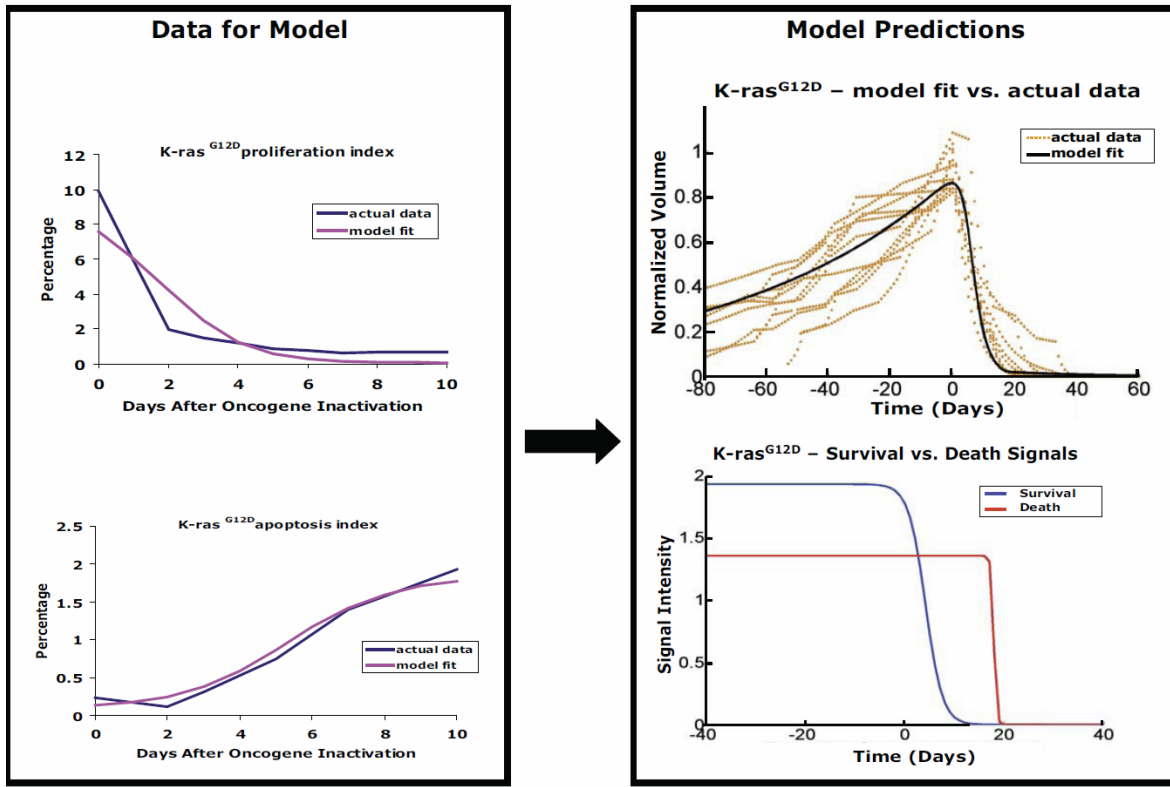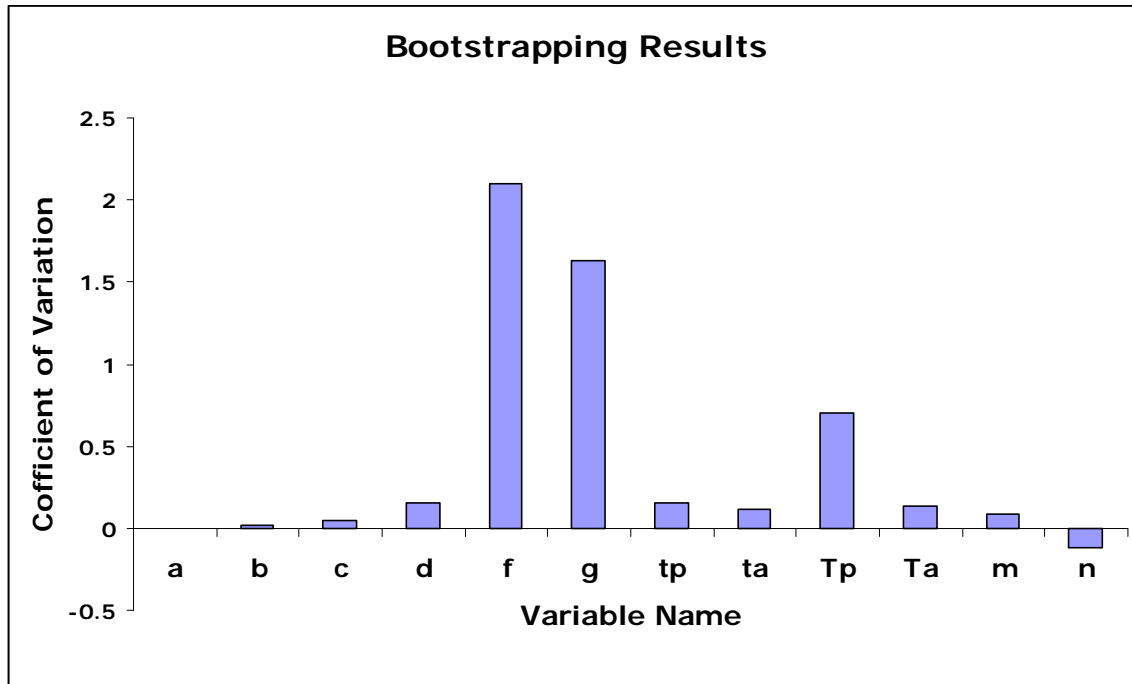
**E**
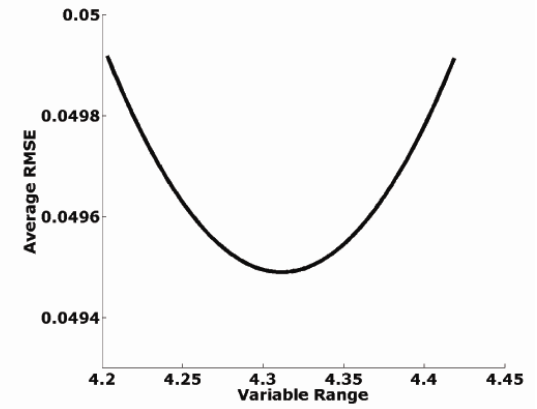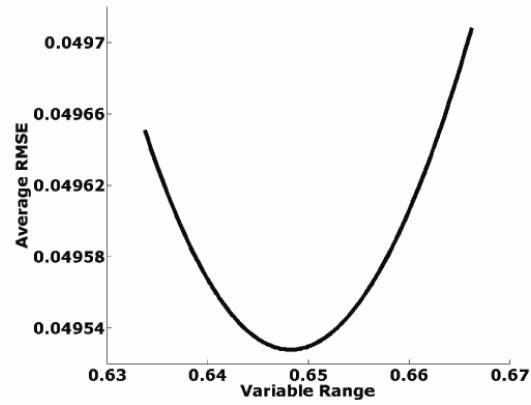
F

G
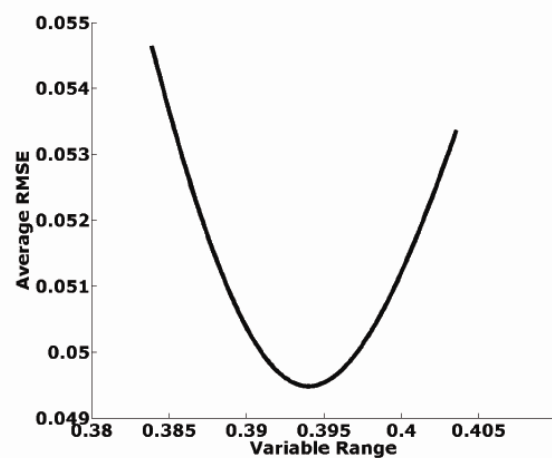
H
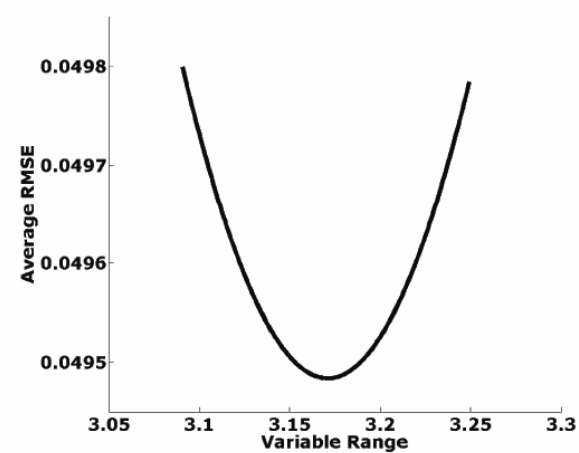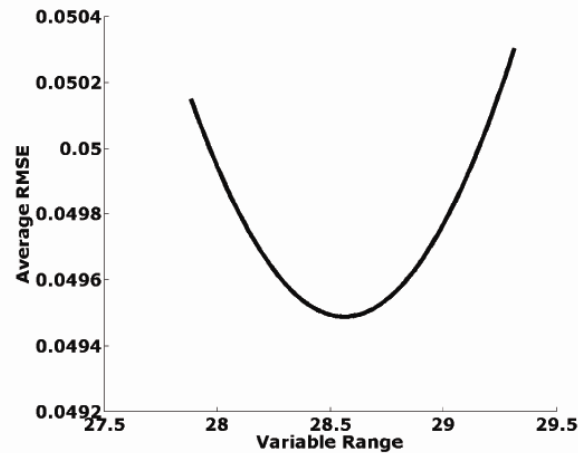
I

Fig. S3. Validation of the ODE mathematical model for oncogene-addicted tumor behavior. Hold-out validation consistently demonstrates differential attenuation of aggregate survival and death signal curves. (A-C) We fixed all parameters, except for a, b, c, d, f, and g, obtained from previous model fitting using all 3 datasets [volumetric measurements (*V*), Ki-67 (*PI*) and cleaved capase3 (*AI*) IHC data). Using different combinations of two of the three datasets, we were able to predict what the signal curves would look like. (A) Apoptosis index (*AI*, cleaved caspase3) and volumetric measurements (*V*) were model fitted to predict the signal curves. (B) Proliferation index (*PI*, Ki-67) and volume data (*V*) were used to predict the signals curves. (C) *PI* and *AI* were used to predict the signal curves. Signal curves predicted from all three combinations are qualitatively concordant and show differential attenuation of the two signals, indicating that our mathematical model is robust. (D) Boostrap resampling of variables used in the mathematical model confirm reproducibility. The bootstrap observational unit is the individual tumor and we used 10,000 bootstrap samples. The results of bootstrapping analysis demonstrated that the proposed variables of our mathematical model are robust to the variation in the data itself and that all parameters are reproducible (within 5% error). Variable names: *a*-starting intensity of the aggregate survival signal; *b*-rate of survival signal decay; *c*-time when survival signals begin dropping off; d-starting intensity of the death signal; *f*-rate of death signal decay; *g*-time when death signals begin dropping off; T_p-duration of intracellular proliferation; T_a-duration of intracellular apoptosis; t_p-duration of proliferation detectable by IHC; t_a-duration of apoptosis detectable by IHC; and *m,n*-thresholds that determine cellular program. (E-I) Sensitivity analysis of the estimated parameters from the Levenberg-Marquardt optimization method demonstrate the precision

of the estimated values. The results showed that all values in our estimated set are at the minimum of the assessed range. (E) All parameters (a-starting intensity of the aggregate survival signal; b-rate of survival signal decay; c-time when survival signals begin dropping off) for survival signals, and (F) similar parameters for aggregate death signals (d, f & g). (G) Durations for intracellular proliferation (T_p, top panel) and apoptosis (T_a, bottom panel). (H) Durations for which proliferation (t_p, top panel) and apoptosis (t_a, bottom panel) can be detected by IHC, and (I) thresholds m (top) and n (bottom) that determine cellular states.

Fig. S4
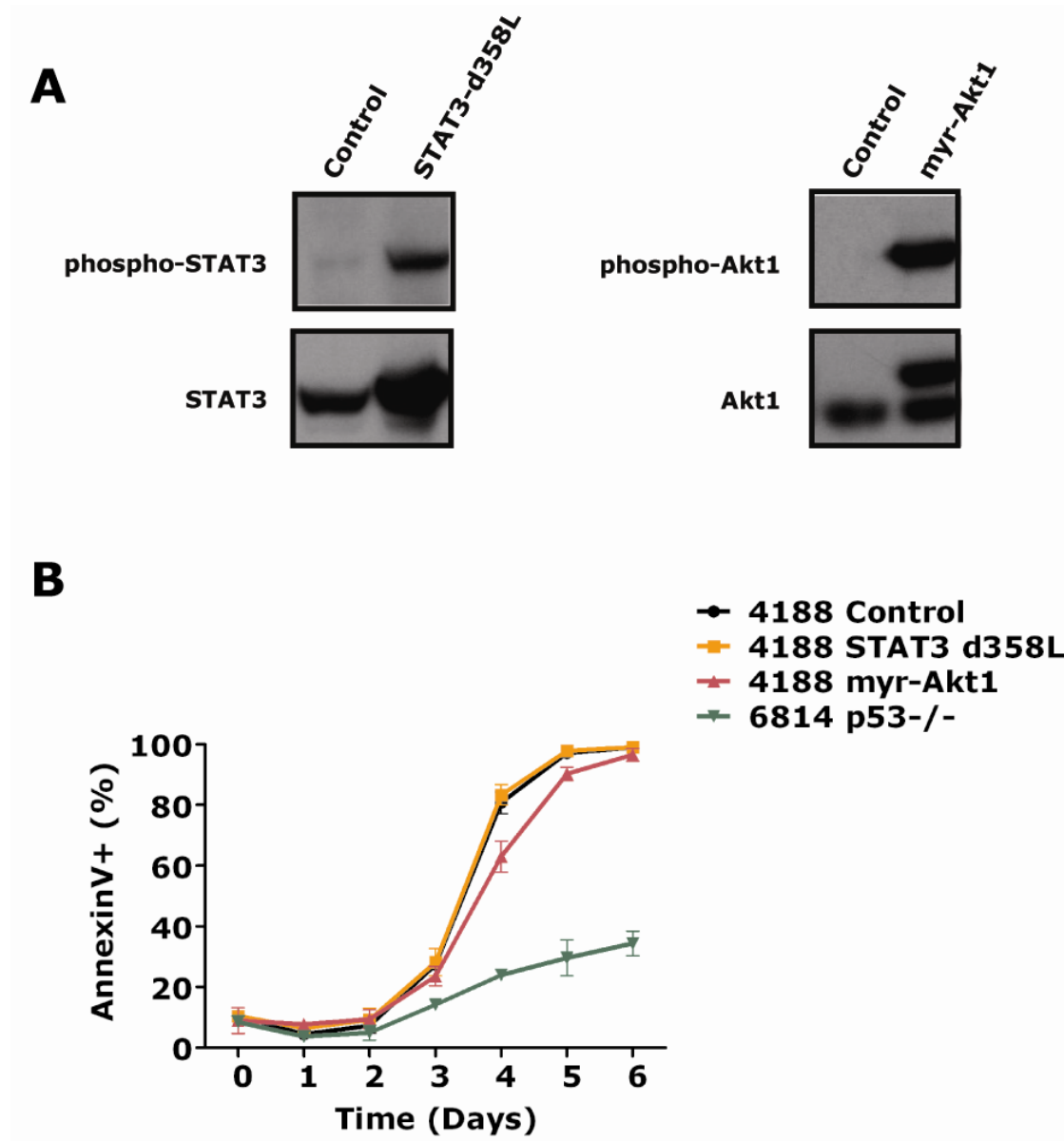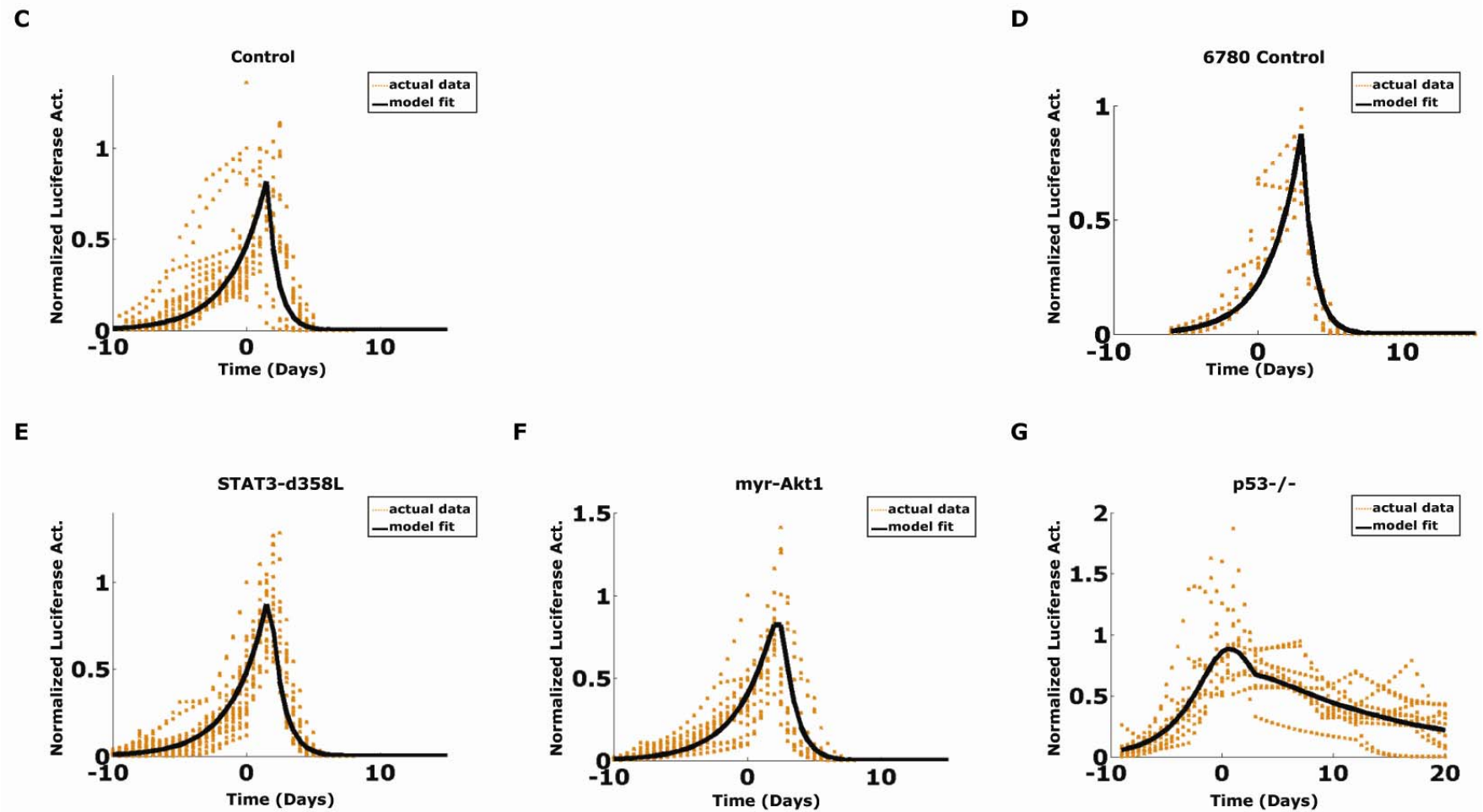
Fig. S4. Genetic perturbation of prosurvival and prodeath pathways in *MYC*-induced lymphomas can impede tumor regression

after *MYC* inactivation in vivo. (A) *MYC*-induced lymphomas were transduced with constructs to express mutant active

forms of Stat3-d358L and myr-Akt1. The resultant lines were checked for expression of Stat3-d358L and myr-Akt1 *via*

phospho-western. (B) A FACS time course using Annexin V staining was performed on the cell lines from (A) and a *MYC*-

induced lymphoma derived from a p53-/- background (6814) following *MYC* inactivation *in vitro*. The myr-Akt1 and p53-/-

MYC-induced lymphomas demonstrate decreased apoptosis beginning on day 3 and at later time points following *MYC*

inactivation in comparison to the control and Stat3-d358L lymphomas. (C-G) Mathematical modeling of *MYC*-induced

lymphomas with bioluminescence imaging (BLI) data demonstrated that genetic perturbations of pro-survival and pro-death

pathways can impede tumor regression following *MYC* inactivation in vivo. The kinetics of tumor regression following

oncogene inactivation was examined in *MYC*-induced lymphomas in the different mutant backgrounds as shown (E-G). Tumor

cell lines labeled with luciferase were transduced with various constructs and then inoculated into syngeneic hosts generating

tumors (numbers of tumors in parentheses). *MYC*-induced tumors were transduced with (C) an empty Control construct (21

tumors); (E) a Stat3-d358L construct (24 tumors); or (F) myr-Akt1 construct (16 tumors). Also, (D) a non-transduced but

luciferase labeled tumor line (5 tumors) was used as a control for (G) a p53-/- *MYC*-induced lymphoma that was labeled with

luciferase (10 tumors). Ten million cells of each variant (E-G) were subcutaneously injected into FVBN mice. Tumor growth

and regression were measured by BLI before and after *MYC* inactivation. Our mathematical model for *K-ras*^{G12D} -induced lung

tumors adapted for BLI (see Supporting Materials and Methods) was able to fit the imaging data: (C) RMSE 12.6%; (D) RMSE 7.0%; (E) RMSE 5.9%; (F) RMSE 5.6%; and (G) RMSE 10.4%.

Fig. S5
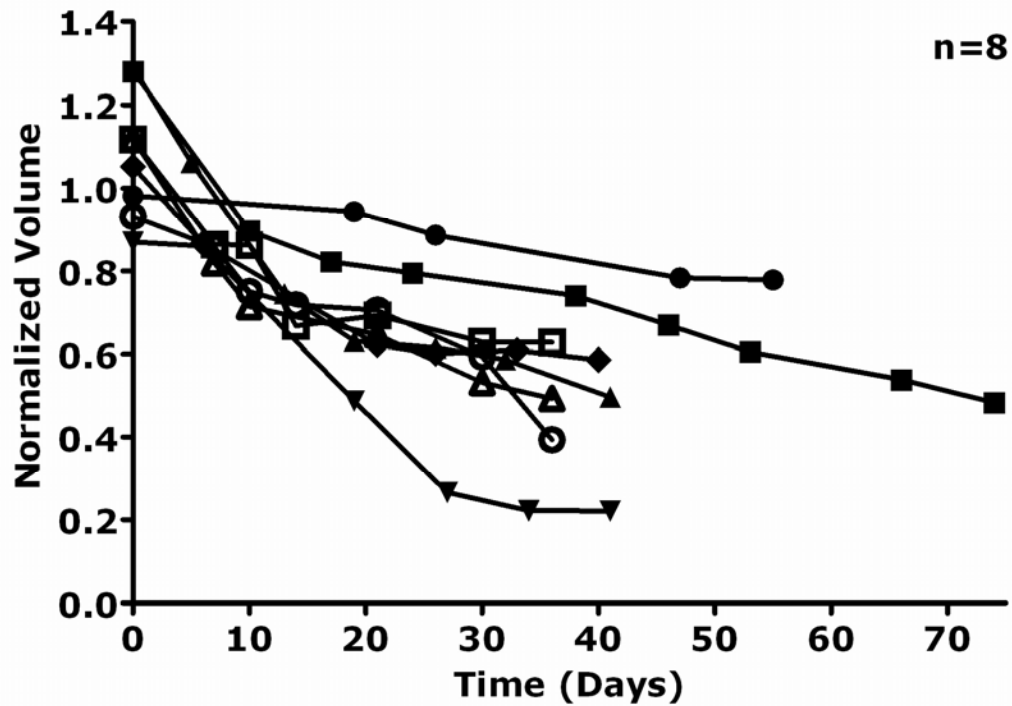
Fig. S5. *MYC*-induced lung tumors are not oncogene-addicted. Volumetric quantization of *MYC*-induced lung tumors following oncogene inactivation using serial microCT with normalization as performed for fig. S2 (described in Supporting Materials and Methods). *MYC*-induced murine lung tumors are oncogene-independent, despite > 6-10 weeks of *MYC* inactivation CM mice still harbor gross tumors (n=8).

Fig. S6
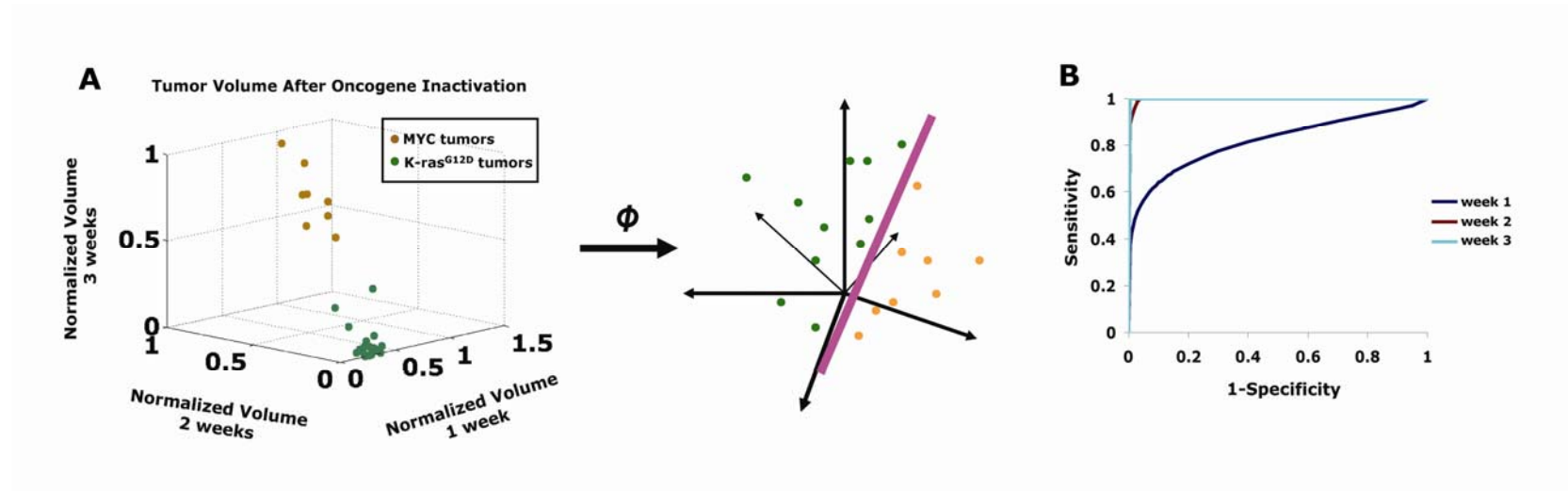
C

After 1 week of inactivation

Predicted	K-ras (%)	MYC (%)
K-ras	19 (0.950)	2 (0.250)
MYC	1 (0.050)	6 (0.750)

After 2 weeks of inactivation

Predicted	K-ras (%)	MYC (%)
K-ras	20 (1.00)	1 (0.125)
MYC	0 (0.00)	7 (0.875)

After 3 weeks of inactivation

Predicted	K-ras (%)	MYC (%)
K-ras	20 (1.00)	0 (0.00)
MYC	0 (0.00)	8 (1.00)

D

After 1 week of inactivation

Predicted	K-ras (%)	Non-K-ras (%)
K-ras	19 (0.950)	6 (0.429)
Non-K-ras	1 (0.050)	8 (0.571)

After 2 weeks of inactivation

Predicted	K-ras (%)	Non-K-ras (%)
K-ras	19 (0.950)	2 (0.143)
Non-K-ras	1 (0.050)	12 (0.857)

After 3 weeks of inactivation

| Predicted	K-ras (%)	Non-K-ras (%)
K-ras	20 (1.00)	2 (0.143)
Non-K-ras	0 (0.00)	12 (0.857)

After 4 weeks of inactivation

Predicted	K-ras (%)	Non-K-ras (%)
K-ras	20 (1.00)	1 (0.071)
Non-K-ras	0 (0.00)	13 (0.929)

Fig. S6. Support vector machine (SVM) trained with quantified imaging data can be used to distinguish *K-ras*^{G12D}- and *MYC*-induced lung tumors. (A) An illustration of the SVM shows that the technique maps the original dataset in 3-D to a higher dimensional space where a maximal separating hyperplane is constructed that best separates the data points between two different genotypes, *K-ras*^{G12D} and *MYC*, for prediction. (B) Receiver operating characteristics (ROC) curves were used to show the accuracy of the SVM technique in predicting the oncogene dependent genotypes based on tumor volumes obtained from different length of time after oncogene targeted therapy. (C-D) Sensitivity and specificity tables for predicting genotype using support vector machine (SVM) trained with serial imaging data from *K-ras*^{G12D} and non-*K-ras*^{G12D} tumors following oncogene addiction. Confusion matrices show the sensitivity and specificity of the SVM technique in predicting the oncogene-dependent genotypes based on the number of tumor volumes measured after oncogene inactivation. The matrices are trained using tumors following simulated targeted therapy from (C) *K-ras*^{G12D} - and *MYC*-induced lung tumors or from (D) *K-ras*^{G12D} - and non-*K-ras*^{G12D} (*MYC* and *MYC*/*K-ras*^{G12D} double animals)-induced lung tumors.

K-ras^G12D – Survival vs. Death Signals
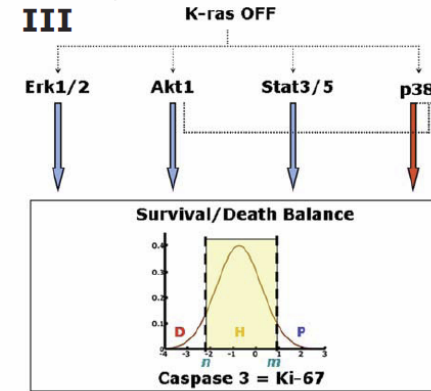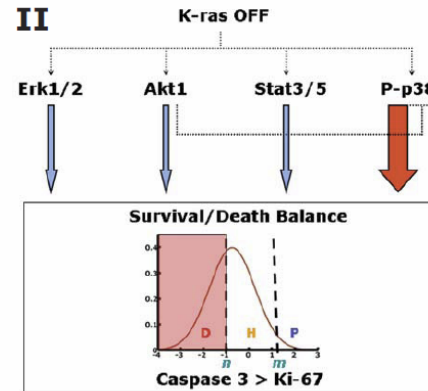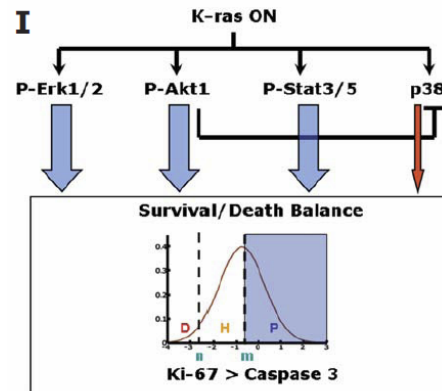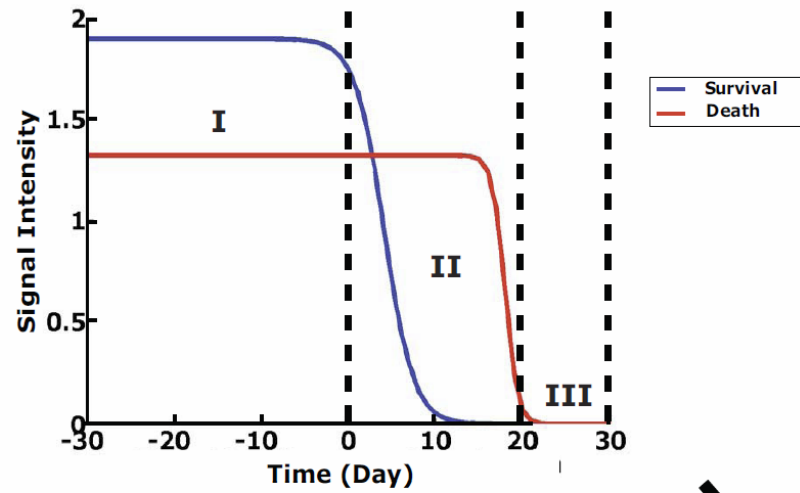
Fig. S7. Schematic integrating the temporal phospho-IHC in relation to $K\text{-}ras^{G12D}$ activation state. The balance of aggregate survival and death signaling determines whether $K\text{-}ras^{G12D}$–induced lung tumors grow, regress or become static. (I) $K\text{-}ras^{G12D}$ signals to Erk1/2, Akt1 and Stat3/5 keeping them phosphorylated denoted by "P-" and width of downstream blue arrows. The pro-death factor p38 is also activated by a signal from $K\text{-}ras^{G12D}$, but negative counter-regulation by phosphos-Akt1 de-phosphorylates p38 (as denoted by a thin downstream red arrow). The integration of aggregate survival and death signals results in the shift of thresholds "m" and "n" in our mathematical model (Fig. 4) resulting in a net preponderance of cells proliferating and therefore net tumor growth. (II) When $K\text{-}ras^{G12D}$ is inactivated Erk1/2, Akt1 and Stat3/5 are quickly de-phosphorylated and negative counter regulation of p38 is released, resulting in transient phosphos-p38 (denoted by a wider downstream red arrow). Similarly, integration of these aggregate survival and death signals results in the shift of thresholds "m" and "n" in our mathematical model (Fig. 4) resulting in a net preponderance of cells dying and therefore net tumor regression. This model is consistent with the delayed attenuation of pro-death factors such as phospho-p38 [larger red arrow as compared to red arrow in panel (I)]. (III) Following a longer period of $K\text{-}ras^{G12D}$ inactivation the aggregate pro-death effectors have decreased as exemplified by p38 (denoted by a thin downstream red arrow) and the net balance is in favor of homeostatic states such as quiescence or differentiation. Width of the blue and red downstream arrows below intracellular mediators is representative of the degree of phospho-IHC signaling observed in Fig. 3A.

References

S1.   S. W. Lowe, E. Cepero, G. Evan, *Nature* **432**, 307 (Nov 18, 2004).

S2.   W.H. Press *et al.,* Numerical Recipes in C: The Art of Scientific Computing (*2ⁿᵈ ed*).
         Cambridge University Press (2002).

S3.   R.G. Renehan, C. Booth, C. S. Potten, *BMJ* **322**, 1536 (2001).

S4.   S. Beer *et al.*, *PLoS biology* **2**, e332 (Nov, 2004).

S5.   P. A. Yushkevich *et al.*, *Neuroimage* **31**, 1116 (Jul 1, 2006).

S6.   D. D. Cody *et al.*, *Invest Radiol* **40**, 263 (May, 2005).

S7.   S. Giuriato *et al.*, *Proceedings of the National Academy of Sciences of the United
         States of America* **103**, 16266 (Oct 31, 2006).

S8. A.N. Basavanhally *et. al. Proceedings of IEEE ISBI* p229 (2010).

S9. D.F.Yankelevitz *et al*., Cancer **97,** 1271 (2003).

S10. R.M. Lindell, *et al*., Radiology **242,** 555 (2007).

S11. S.Y. El Sharouni, et. al. Br J Cancer **89,** 2184 (2003).

Supplementary Videos: (A) Regression of K-ras^{G12D} -induced lung tumors imaged serially using μCT. Movie of CR lung tumors before inactivation of K-ras^{G12D} by withdrawal of doxycycline is representative of 11 CR lung tumor bearing mice serially scanned by microCT as described in the Supporting Materials and Methods (AVI; 1.7 MB). (B) Regression of K-ras^{G12D} -induced lung tumors imaged serially using microCT. Movie of CR lung tumors after inactivation of K-ras^{G12D} by withdrawal of doxycycline is representative of 11 CR lung tumor bearing mice serially scanned by microCT as described in the Supporting Materials and Methods (AVI; 1.3 MB).